Volume 2, Number 3 *September 2020*

Nanomaterials Science & Engineering

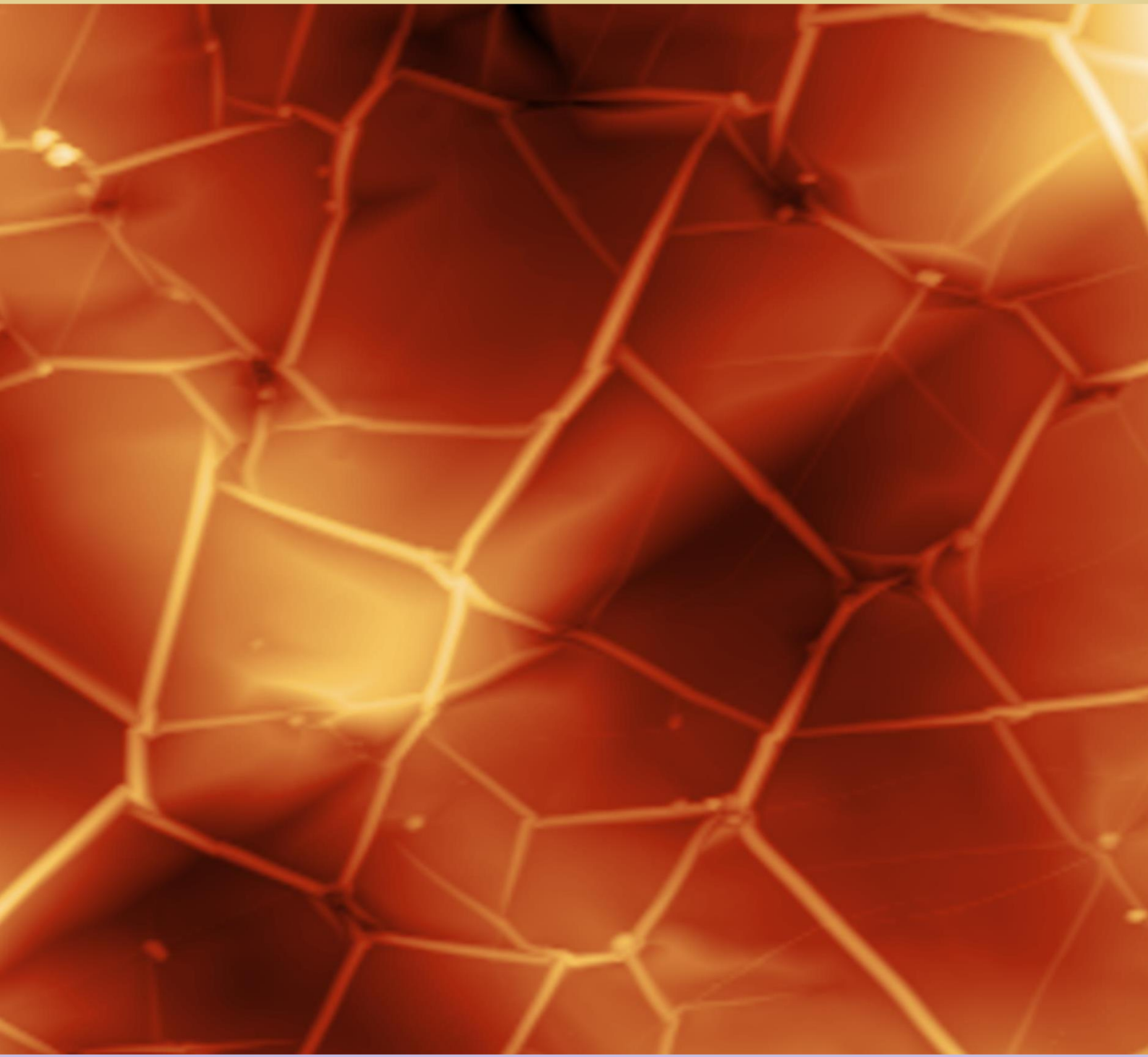

university of aveiro tema centre for mechanical technology and automation

Volume 2, Number 3 *September 2020*

Nanomaterials Science & Engineering

university of aveiro tema centre for mechanical technology and automation

Title
Nanomaterials Science & Engineering (NMS&E), Vol.2, No.3, 2020

Cover and Logo
Igor Bdikin, Manoj K. Singh (Graphene/Ni, AFM image, 15x15x0.5 μm^3)

Publisher
University of Aveiro

Support
Serviços de Biblioteca, Informação Documental e Museologia
Centre for Mechanical Technology & Automation (TEMA)
Mechanical Engineering Department
University of Aveiro

Mailing Address
Department of Mechanical Engineering
University of Aveiro
Aveiro 3810-193
Portugal
E-mail: bdikin@ua.pt

ISSN: 2184-7002

NANOMATERIALS SCIENCE & ENGINEERING
Vol. 2, No. 3, pp. 103-112 (2020)

RESEARCH ARTICLE

https://doi.org/10.34624/nmse.v2i3.11179

2nd International Conference on Nanomaterials Science and Mechanical Engineering
University of Aveiro, Portugal, July 9-12, 2019

Free vibration investigation of single walled carbon nanotubes with rotary inertia

Abdelkadir Belhadj*, Abdelkrim Boukhalfa, Sid. A. Belalia

Computational Mechanics Laboratory, Department of Mechanical Engineering, Faculty of Technology, University of Tlemcen, Tlemcen, Algeria

**Corresponding author, e-mail address: belhabdelkadir@gmail.com*

Received 31 December 2019; accepted 15 September 2020; published online 22 September 2020

ABSTRACT

In present work, the free vibration dynamics of rotating single walled carbon nanotubes is investigated by using Eringen's nonlocal theory of elastic structures. Transverse flexural vibration of SWCNT embedded in an elastic medium, a rotating cantilever SWCNT and a nanorotor based SWCNTs is elaborated by using the Hamilton principle to obtain governing equations. Generalized differential quadrature method (GDQM) is employed to discretize and resolve the Eigen problem.

The effect of small scale, boundary conditions and angular velocity on the dynamic parameters is studied. Obtained results showed that SWCNTs provide exceptional structural properties. Findings of this study can be involved in the design of next generation nanomachines and nano-devices.

1. INTRODUCTION

Carbon nanotubes (CNT's) are the main subject of research in nanotechnology; developed by Lijima [1] using transmission electron microscopy, the research interest in CNT's has been enhanced by introducing them in nanoelectromechanical systems (NEMS) [2], this interest in CNTs is due the exceptional mechanical, chemical, electrical, thermal and optical properties that they offer. CNT's are increasingly being used as building parts of nano-machines such as nano-robots, nano-devices, nano-sonsors and nano-actuators for NEMS, as strong reinforcement nanomaterials for nano-composite materials, as biological nanobots for drug delivery and therapy.

Researches on structural dynamics of nanoscale materials used to involve molecular dynamic (MD) simulation to investigate the nano-effect with accurate solutions for CNT's with small deflection. However, MD is limited to a number of atoms 10^9 and it required a high cost computation. In recent years, elastic continuum models are employed as effective and successful theories to study mechanical and physical properties of CNT's [3, 4]. Nonlocal elasticity theory [5] models has been extensively used to model CNTs to study the nanoscale effects. In this theory, the small scale effects are captured by assuming that the stress at a point is a function not only of the strain at that point but also a function of the strains at all other points of the domain. Various works related to nonlocal elasticity theory are found in several references. Soltani et al. [6] considered the nonlocal Euler-Bernoulli elastic beam theory to investigate the vibrational behavior of a single-walled carbon nanotubes (SWCNTs) embedded in an elastic medium. Both Winkler-type and Pasternak-type models are employed to simulate the interaction of the SWNTs with a surrounding elastic medium more accurately, they showed that the stiffness of the medium due to both Pasternak-

type and Winkler-type increases, the bending stiffness, and the associated resonant frequency increases, consequently. Jena and Chakraverty [7] investigated the free vibration of SWCNT resting on exponentially varying Winkler elastic foundation by using DQM, they showed the effect of non-uniform parameter, nonlocal parameter, aspect ratio, Winkler modulus parameter and boundary condition on the frequency parameter.

The vibration behavior study of SWCNT's in rotation as cantilever beams has known a great interest by researchers, Narendar [8] studied the flapwise bending free vibration of a rotating cantilever SWCNT. He showed that angular velocity parameter has increased the frequency parameter, and that the nonlocal parameter effects the first mode frequency parameter increasingly and the second mode frequency parameter decreasingly.

Belhadj et al. [9] studied the SWCNT nanostructure as a rotating nanoshaft, they investigated the effect of nonlocal parameter, boundary conditions and angular velocity on the frequency by showing the Campbell diagram to evaluate critical angular velocities.

The objective of this study is to investigate the transverse vibratory behavior of SWCNT under different dynamic conditions. A nonlocal elastic Euler-Bernoulli beam model was used to study the SWCNT first in surrounding Winkler type elastic foundation, then this nanostructure was studied as a rotating cantilever beam and finally under axial rotating inertia as a nanoshaft to examine their behavior as nano-rotors for next generation rotating nano-machinery applications [10].

2. ERINGEN'S THEORY OF NONLOCAL ELASTICITY

Eringen [11] has introduced the theory of non-local elasticity to account for the small-scale effect. Unlike the classical theory of elasticity, the non-local theory consider long-range inter-atomic interaction and yields results dependent on the size of a body. In the following, the simplified form of the Eringen's nonlocal constitutive equation is employed:

$$(1-(e_0 a)^2\nabla^2)\sigma^{nl}=\sigma^{l}$$

where ∇^2 is the Laplacian operator, $(e_0 a)^2$ is nonlocal parameter,

a - internal characteristic length,
e_0 - constant,
nl - non local,
l - local.

3. TRANSVERSE VIBRATION OF SWCNT

In the present paper, a single walled carbon nanotube designed using Nanotube Modeller (Figures 1, 2 and 3) is modelled mathematically based on Euler-Bernoulli beam model. The displacement field of at a point of the beam can be expressed as:

$$u_x(x,t)=u(x,t)-z\frac{\partial w(x,t)}{\partial x} \quad (1)$$

$$u_y(x,t)=0 \quad (2)$$

$$u_z(x,t)=w(x,t) \quad (3)$$

$u_x(x,t)$, $u_y(x,t)$ and $u_z(x,t)$ are the axial and the transverse displacement component at the mid-plane respectively. The linear strain-displacement relations for the curved Euler-Bernoulli beam are expressed as:

$$\varepsilon_{xx}=\frac{\partial u}{\partial x}-z\frac{\partial^2 w}{\partial x^2} \quad (4)$$
$$\varepsilon_{zz}=\varepsilon_{xz}=0$$

According to the nonlocal elasticity theory it is assumed that the stress at a point is a function of strains at all points in the continuum. the nonlocal constitutive behaviour of a Hooken solid is represented by the following differential constitutive relation:

$$[1-(e.a)^2\nabla^2]\sigma^{nl}=\sigma^{l} \quad (5)$$

where ∇^2 is the Laplacian operator, $(e.a)^2$ is the nonlocal parameter.
a - internal characteristic length,
e_0 - constant,
nl - non local,
l - local.

The equation of motion of free vibration of a single walled carbon nanotube (SWCNT) is obtained after deriving the governing equations using Hamilton's principle as:

$$\rho A\frac{\partial^2 w}{\partial t^2}+EI\ \frac{\partial^4 w}{\partial x^4}=0 \quad (6)$$

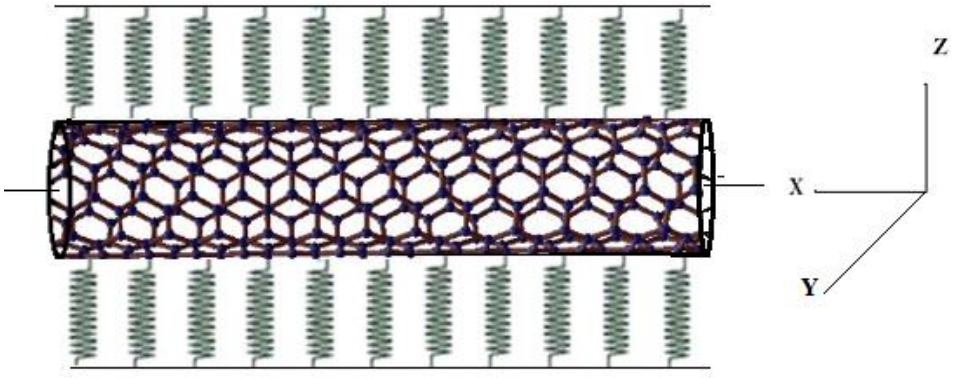

Figure 1. SWCNT embedded in an elastic medium.

w (x,t) is the transverse deflection of the SWCNT, *E*, *I* and *A* are the elastic modulus, the moment of inertia, and the cross section respectively. Assumption the nanotube has a constant cross section, the equation (6) can be written as:

$$\phi^{(4)}(x) - \beta^4 \phi(x) = 0 \quad (7)$$

Where $\phi(x)$ is the mode shape (Eigen-shape)

$$\beta^4 = \frac{\rho A \omega^2}{EI} \quad (8)$$

The analytical solution of the equation (7) is

$$\phi(x) = C_1\, sin(\beta x) + C_2\, cos(\beta x) + C_3 sinh(\beta x) + C_4 cos(\beta x) \quad (9)$$

C_1, C_2, C_3 and C_4 are the constants depending on boundary conditions.

3.1. SWCNTs embedded in an elastic medium

In this section, the SWCNT is considered to be embedded in an elastic medium of Winkler- type elastic foundation (Figure 1).
By introducing the elastic medium, the equation (6) become:

$$\rho A \frac{\partial^2 w}{\partial t^2} + EI\, \frac{\partial^4 w}{\partial x^4} = P(x) \quad (10)$$

P(x) is the pressure acting on the CNT due to the surrounding elastic medium which is opposite to the deflections of CNT,

$$P(x) = -kw \quad (11)$$

k: is the spring constant relative to the elastic medium described as a Winkler-type elastic foundation.
By introducing the non-local elasticity theory, we obtain the following governing equation:

$$\rho A \left[\frac{\partial^2 w}{\partial t^2} - (e_0 a)^2 \nabla^2 \frac{\partial^2 w}{\partial t^2}\right] + EI\, \frac{\partial^4 w}{\partial x^4} + K[w - (e_0 a)^2 \nabla^2 w] = 0 \quad (12)$$

Where:

$$w(x,t) = W.e^{i\omega t}$$

In order to investigate the dynamic parameters we rewrite the governing equation in a dimensionless form by introducing the following no dimensionless quantities:

$$\Omega^2 = \frac{\rho A \omega^2 L^4}{EI},\ \ \bar{K} = \frac{kL^4}{EI},\ \ \mu = \frac{e_0 a}{L}, \xi = \frac{x}{L}$$

3.2. SWCNTs as a rotating cantilever beam

In this section, a rotating cantilever nanobeam based SWCNT is studied (Figure 2). Flexural vibration equation based on the bending moment *M* and the shear force *Q* are expressed as:

$$\frac{\partial Q}{\partial x} = \rho A \ddot{u} \quad (13)$$

$$\frac{\partial M}{\partial x} + \left(T(x)\frac{\partial w}{\partial x}\right) = \rho A \ddot{w} \quad (14)$$

With $Q = \int_A \sigma_{xx}\, dA$

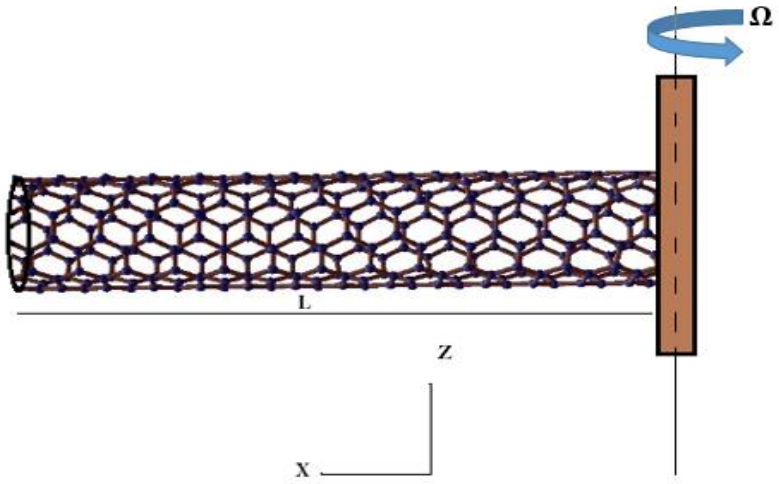

Figure 2. SWCNT as a rotating cantilever beam

$$M = \int_A z\,\sigma_{xx} dA \quad (15)$$

T(x) the axial force due to centrifugal stiffening:

$$T(x) = \int_x^L \rho A \Omega^2 (x + R) dx \quad (16)$$

By applying nonlocal elastic theory, we obtain:

$$Q - (e_0 a)^2 \frac{d^2 Q}{dx^2} = EA \frac{du}{dx} \quad (17)$$

$$M - (e_0 a)^2 \frac{d^2 M}{dx^2} = EI \frac{d^2 w}{dx^2} \quad (18)$$

The following nondimensional parameters are employed to execute the investigation:

$\Omega^2 = \frac{\rho A \omega^2 L^4}{EI}$, $\mu = \frac{e_0 a}{L}$, $\xi = \frac{x}{L}$

The angular velocity parameter $\gamma^2 = \frac{\rho A \Omega^2 L^4}{EI}$ the hubradius $\delta = \frac{x}{L}$

3.3. SWCNTs as a rotating shaft

A SWCNT structure (Figure.3) is modelled via Euler-Bernoulli beam theory under rotating inertia, its governing equations are derived based on Hamilton's principle that considers the motion of an elastic structure during time is reduced to zero by

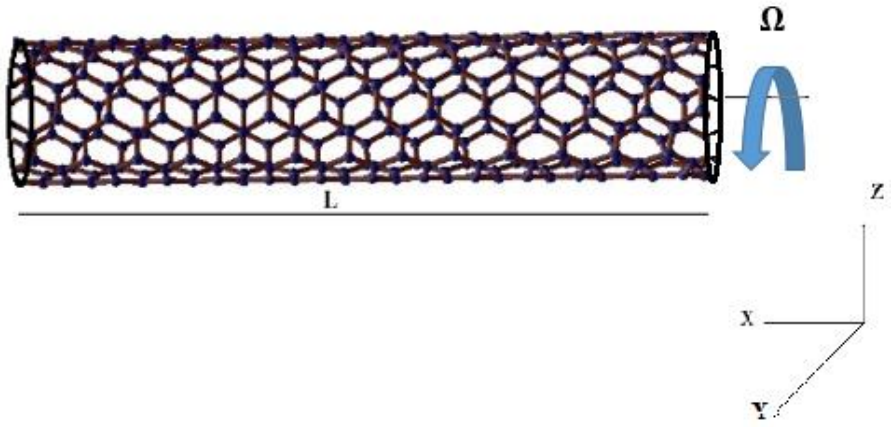

Figure 3. Geometry of a spinning SWCNT shaft.

combining the virtual displacements and virtual forces.

$$\int_{t1}^{t2}(\delta U + \delta V - \delta K)dt = 0 \quad (19)$$

Where:

$$\delta U = \int_0^L \left(N_{xx}\frac{\partial \delta u}{\partial x} - M_y\frac{\partial^2 \delta v}{\partial x^2} - M_z\frac{\partial^2 \delta w}{\partial x^2}\right)dx \quad (20)$$

is the variation of the strain energy. Whereas the variation of kinetic energy is:

$$K = \frac{1}{2}\int_0^L \begin{Bmatrix} \rho A\left[\dot{u}\frac{\partial \delta u}{\partial t} + \dot{v}\frac{\partial \delta v}{\partial t} + \dot{w}\frac{\partial \delta w}{\partial t}\right] + \\ \rho I\left\{\frac{\partial^2 v}{\partial t \partial x}\frac{\partial^2 \delta v}{\partial t \partial x} + \frac{\partial^2 v}{\partial t \partial x}\frac{\partial^2 \delta v}{\partial t \partial x}\right\} + \\ 2\Omega\left(\frac{\partial \delta \dot{v}}{\partial x}\frac{\partial w}{\partial x} - \frac{\partial \delta \dot{w}}{\partial x}\frac{\partial v}{\partial x}\right) + 2\Omega^2 \end{Bmatrix} dx \quad (21)$$

ρ is the mass density, A is the cross section, I is the moment of inertia about cross section, and Ω is the angular velocity of the rotating nanostructure.

By applying the theory of nonlocal elasticity, we obtained:

$$\rho A\left[\ddot{u} - (e.a)^2\frac{d^2\ddot{u}}{dx^2}\right] = EA\frac{d^2u}{dx^2} \quad (22)$$

$$\rho A\left[\ddot{v} - (e.a)^2\frac{d^2\ddot{v}}{dx^2}\right] + \rho I\left[\dot{v} - (e.a)^2\frac{d^2\dot{v}}{dx^2}\right] - 2\Omega\left(\dot{w} - (e.a)^2\frac{d^2\dot{w}}{dx^2}\right) = EI\frac{d^4v}{dx^4} \quad (23)$$

$$\rho A\left[\ddot{w} - (e.a)^2\frac{d^2\ddot{w}}{dx^2}\right] + \rho I\left[\dot{w} - (e.a)^2\frac{d^2\dot{w}}{dx^2}\right] + 2\Omega\left(\dot{v} - (e.a)^2\frac{d^2\dot{v}}{dx^2}\right) = EI\frac{d^4w}{dx^4} \quad (24)$$

Where, the three-directional deflection is defined as:

$$u(x,t) = ue^{i\omega t}\ , v(x,t) = ve^{i\omega t}\ , w(x,t) = we^{i\omega t}$$

4. APPLICATION OF GENERALIZED DIFFERENTIAL QUADRATURE METHOD (GDQM)

Bellman et al. [12] have firstly introduced differential quadrature method, a new partial technique called generalized differential quadrature method (GDQM) was proposed by Shu and Richard [13] to solve applied mechanics problems. In this paper, GDQM is used to discretize the differential equations.

The philosophy of DQM is based on computing the derivatives of the functions constituting the governing equation. Each derivative is formulated by a sum of values at its neighboring points.

$$\left|\frac{d^n f}{dx^n}\right|_{x=x_i} = \sum_{j=1}^N {C_{ij}}^{(n)} f(x_j) \qquad i = 1,2,\dots N; n = 1,2,\dots N-1 \quad (25)$$

Where ${C_{ij}}^{(n)}$ is the weighting coefficient of the *nth* order derivative, and *N* the number of grid points of the whole domain, $(a = x_1, x_2, \dots x_i, \dots x_N = b)$.

According to Shu and Richard rule [13], the weighting coefficients of the first-order derivatives in direction ξ, $(\xi = \frac{x}{L})$ are determined as:

$$\begin{aligned} {C_{i,j}}^{(1)} &= \frac{P(\xi_i)}{(\xi_{i-}\xi_j).P(\xi_j)} \quad i,j = 1,2\dots N\ , i \neq j \\ {C_{i,j}}^{(1)} &= -\sum_{\substack{j=1 \\ j\neq i}}^N {C_{i,j}}^{(1)} \end{aligned} \quad (26)$$

Where: $P(\xi_i) = \prod_{j=1}^N (\xi_{i-}\xi_j) \quad i \neq j$

The second and the higher order derivatives can be computed as:

$${C_{i,j}}^{(2)} = \sum_{k=1}^N {C_{i,k}}^{(1)}.{C_{k,j}}^{(1)} \qquad i = j = 1,2\dots N. \quad (27)$$

$${C_{i,j}}^{(r)} = \sum_{k=1}^N {C_{i,k}}^{(1)}.{C_{k,j}}^{(r-1)} \qquad i = j = 1,2\dots N.$$
$$\mathrm{r} = 2,3\dots \mathrm{m}\ (\mathrm{m} < \mathrm{N})$$

Throughout the paper, the grid pints are assumed based on the well-established Chebyshev-Gauss-Lobatto points

$$\xi_i = \frac{1}{2}\left(1 - cos\frac{(i-1)\pi}{N-1}\right) \quad i = 1,2\dots N \quad (28)$$

the boundary conditions used for the free vibration of rotating nonlocal shaft are:

Simply supported beam

$$w(\xi = 0) = \frac{\partial^2 w(\xi=0)}{\partial \xi^2} = 0 \ \text{ and } \ w(\xi = 1) = \frac{\partial^2 w(\xi=1)}{\partial \xi^2} = 0 \quad (29)$$

Clamped-Clamped beam

$$w(\xi = 0) = \frac{\partial w(\xi=0)}{\partial \xi} = 0 \quad \text{and} \quad w(\xi = 1) = \frac{\partial w(\xi=1)}{\partial \xi} = 0 \tag{30}$$

Simply supported-Clamped beam

$$w(\xi = 0) = \frac{\partial^2 w(\xi=0)}{\partial \xi^2} = 0 \quad \text{and } w(\xi = 1) = \frac{\partial w(\xi=1)}{\partial \xi} = 0 \tag{31}$$

5. RESULTS AND DISCUSSIONS

In this section, results of our study are reported here after solving a complex Eigen problem by developing a Matlab code using GDQM technique. The nonlocal governing differential equation is solved using sufficient numbers of grid points which is taken as 15 as prove our previous studies. The effects of elastic medium, of small-scale parameter or nonlocal parameter, lower and higher angular velocities are investigated and the related graphs are plotted. For the present study, the properties of the nonlocal nanobeams are considered that of a SWCNT. An armchair SWCNT with chirality (5,5) is considered. With a Young's modulus E=2.1 TPa, the length- radius ration is taken as L=80d, d=1nm, a density ρ=7800kg/m^3,and a moment of inertia I=πd^4/64.

The validation of our results have been insured by comparing the flexural frequency parameters with Chakraverty [14] results for simply supported beam simply supported beam. Table 1 shows that the first four frequency parameters computed by as

Table 1. Comparison of First four frequency parameters of Euler-Bernoulli nanobeam for different boundary conditions and scaling effect parameters.

	$\mu^2 = 0$		$\mu^2 = 0.3$		$\mu^2 = 0.5$	
	Present	Chakraverty[14]	Present	Chakraverty	Present	Chakraverty
SS	3.1416	3.1416	2.6800	2.6800	2.3022	2.3022
	6.2832	6.2832	4.3013	4.3013	3.4404	3.4604
	9.4243	9.4248	5.4413	5.4422	4.2885	4.2941
	15.5035	15.5665	6.3646	6.3633	4.9731	4.9820

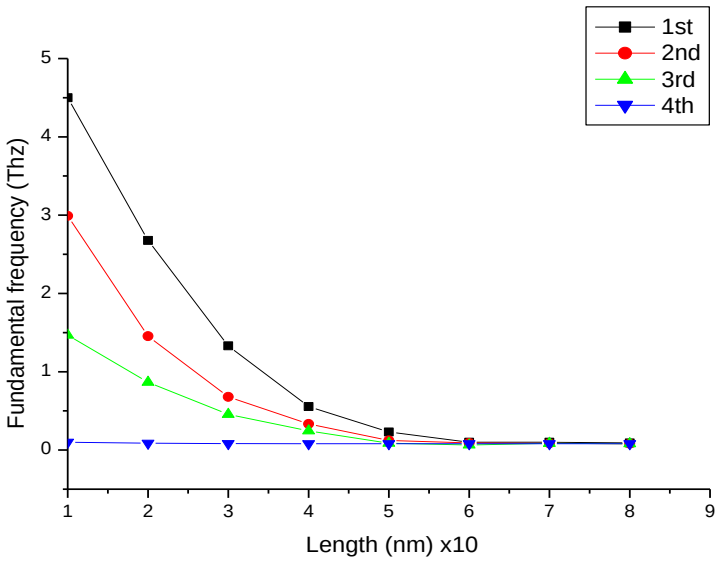

Figure 4. First four natural frequencies versus the length.

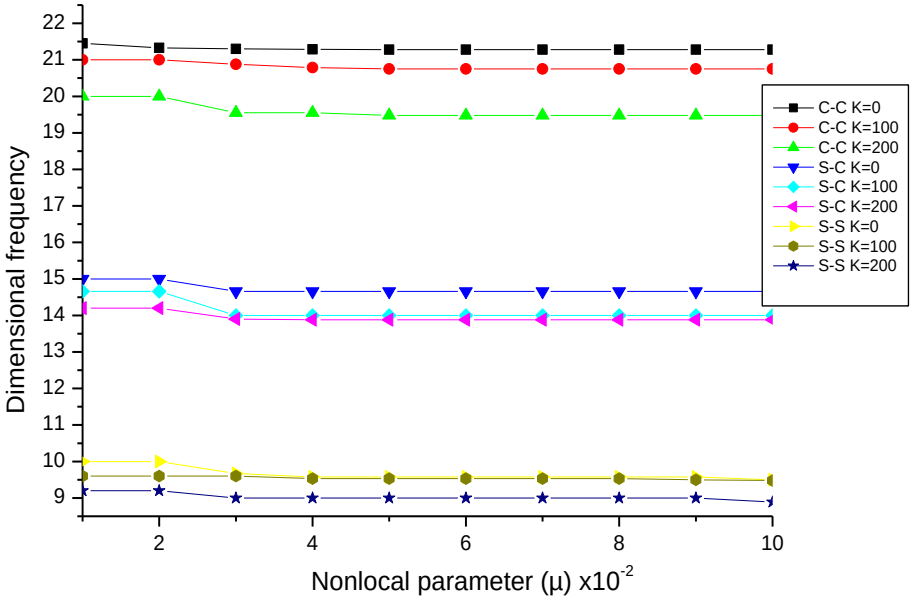

Figure 5. Variation of frequency parameters with nonlocal parameter for different elastic foundations.

present good agreement with those cited in literature.

5.1. SWCNT embedded in an elastic foundation

For the SWCNT resting on Winkler elastic foundation, natural frequencies are computed and valuated to be considerably higher (Tera-hertz) due to exceptional mechanical properties that offer CNTs. The figure 4 shows the first four natural frequencies along the SWCNT for a simply supported-clamped beam boundary condition, it is remarkable that the four frequencies are distinguished in the beginning of the nanobeam, and they are converged in the end of the SWCNT. Whereas the first fundamental frequency is approximatively, uniform.

The figure.5 illustrates the effect of non-local parameter on the vibrational dimensionless frequency response for different boundary conditions, it shows that the frequency response for Clamped-Clamped beam is higher than that of simply supported-clamped and simply supported beam. The frequency response for a spring constant $\overline{K}$ null is higher than that with a higher $\overline{K}$, which improves the inverse relationship between the dimensionless frequency Ω and $\overline{K}$.

5.2. SWCNT as a rotating cantilever nanobeam

For rotating cantilever nanobeam, as the angular velocity parameter increases the fundamental frequency parameter also increases. This observation is found to be similar for both the local and nonlocal elastic models. The increase in frequency with angular velocity is attributed to the stiffening effect of the centrifugal force, which is directly proportional to the square of the angular velocity. These remarks are valid only for the fundamental frequency parameter (Figure 6) where the frequency parameter increases with the increase of both angular velocities parameters and nonlocal parameters. For the higher mode frequency parameter, these remarks are invalid.

Figure 7 shows that the second mode frequency parameters are increasing when the angular velocity parameters increase but they decrease when the nonlocal elastic parameter increases. The small scale effect on the vibration response is amplified at high angular velocity of SWCNT. The higher frequency at amplified zone is due to the coupling effect of both rotational speed and nonlocal parameter.

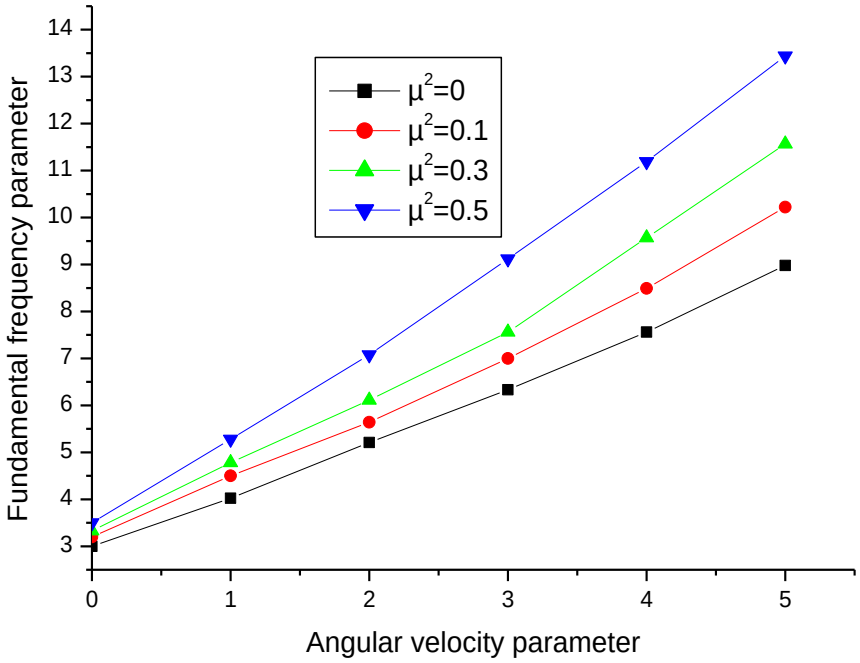

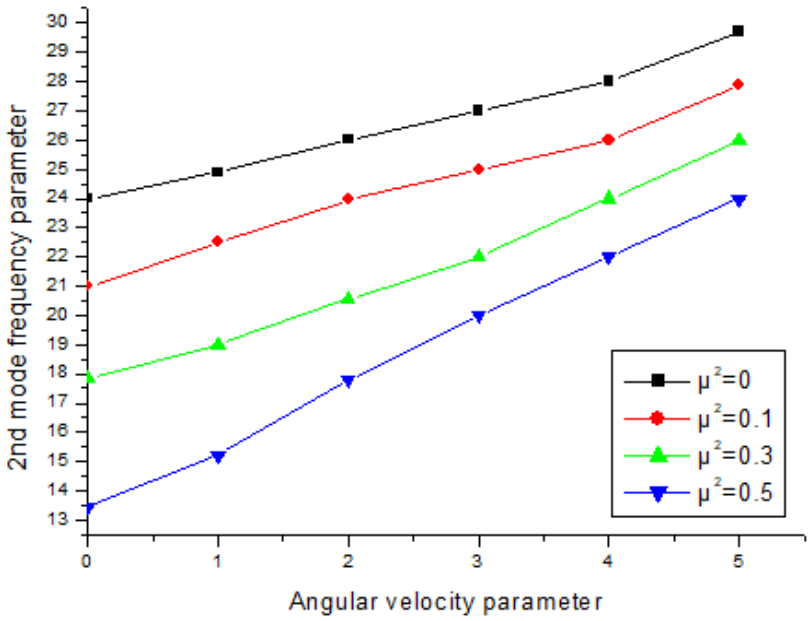

Figure 7. First frequency parameter versus angular velocity.

5.3. SWCNT as a rotating nanoshaft

In this section, the rotation of the SWCNT nanobeam is considered. The investigation of the vibration behaviour of the nanorotor [15] will be done by solving the global Eigen problem expressed as:

$$(-\lambda^2[M] + j\lambda[G] + K).(U, V, W)^T = 0 \qquad (25)$$

G is the gyroscopic matrix, j^2=-1.

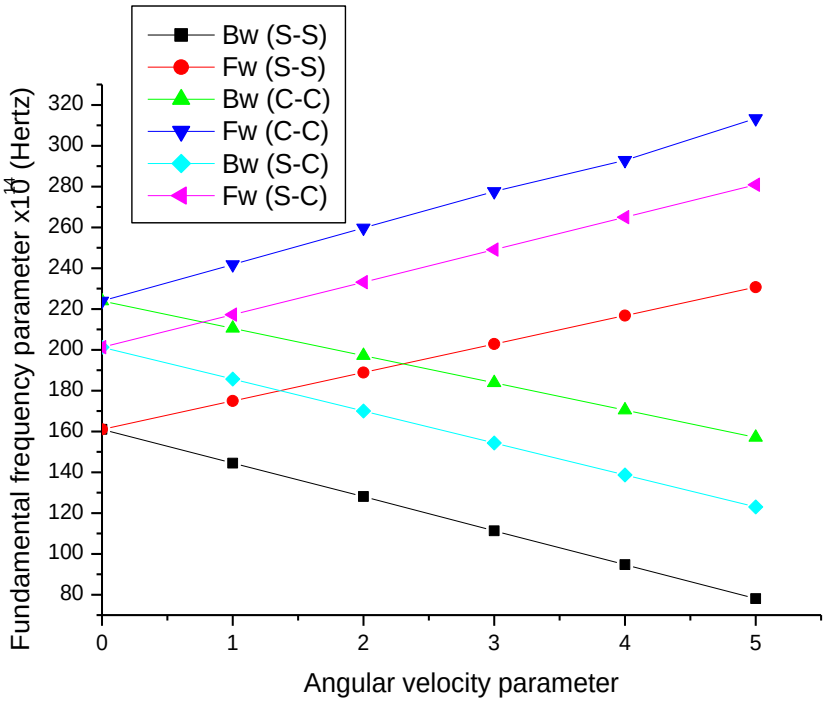

Figure 8. First frequency parameter versus angular velocity.

The Campbell diagram is employed to determine the critical speed λ_{Cr} where the nanorotor vibrates violently, it is the rotating speed correspondent to the intersection of the frequency curves and the angular velocities curves(λ=γ).

Figure 8 shows the Campbell diagram for different boundary conditions for a nonlocal nanobeam μ^2=0.3. It is showed that the fundamental frequency have a linear relationship with angular velocities, the angular velocity parameters have increased the fundamental frequencies; the increasing frequency is the forward frequency, whereas the decreasing one is the backward frequency. It is also remarked that the C-C frequencies are higher than those of SS-C and SS boundary conditions, this difference in results is due to the effect of boundary conditions on the stiffness matrix that changes the eigenvalue decomposition of the system matrix.

5. CONCLUSION

In this paper, a computational structural dynamic analysis based on Eringen's elastic constitutive model is done to investigate the free vibration of SWCNT nanostructure under three structural dynamic situations: first this nanostructure is studied resting on an elastic foundation of Winkler type, second the nanostructure is examined rotating around its transverse axis as a cantilever beam, then rotating as a nanoshaft around its axial axis.

The discretisation and the resolution of governing equations of motion that are derived based on Hamilton principles, is worked out by using the semi-analytical technique, generalized differential quadrature method (GDQM) that is highly recommended for structural nanomechanical problems.

Results obtained from this study are summarized as following:

- At nanoscale, nonlocal elasticity with other non-classical elastic theories are employed to model the problem.
- CNT's offer exceptional mechanical properties that are highly required in nanotechnology applications, in particularly next generation rotating nano-machinery.

- For SWCNT resting in elastic foundations, the elastic medium decreases their frequency parameters.
- For rotating cantilever nanobeam, angular velocity parameter increases the fundamental frequency parameter, so the nonlocal parameter does for fundamental frequency. A high order mode of vibration inversed the effect of nonlocal parameter.
- For the SWCNT nanorotor, Rotary inertia of the SWCNT nanostructure have split the frequency parameter to forward and backward frequencies (Campbell diagram).
- The increased critical speed parameter influences the forward frequency parameter increasingly and the backward frequency parameter decreasingly. The small scale parameter has a significant effect on the dynamic parameters, it decreases the frequency parameters as it increases.

REFERENCES

[1] S. Iijima, Helical Microtubules of graphitic carbone, *Nature* **345**, 56-58 (1991).

[2] K.L. Ekinci, M.L. Roukes, Nanoelectromechanical systems, *Rev. Sci. Insr.* **76**, 061101 (2005).

[3] J.P. Lu, Elastic properties of carbon nanotubes and nanoropes, *Phys. Rev. Lett.* **79**, 1297 -1300 (1997).

[4] P.R. Bandaru, Electrical properties and applications of carbon nanotube structures, *J. Nanosci. Nanotechnol.* **7(1)**, 1239-1267 (2007).

[5] A.C. Eringen, ON DIFFERENTIAL-EQUATIONS OF NONLOCAL ELASTICITY AND SOLUTIONS OF SCREW DISLOCATION AND SURFACE-WAVES, *J. Appl. Phys.* **54**, 4703 (1983).

[6] P. Soltani, H. A. Dastjerdi, A. Farshidianfa, Vibration of wavy single-walled carbon nanotubesbased on nonlocal Euler Bernoulli and Timoshenko models, *Int. J. Adv. Struct. Eng.*, 4 (3), (2012).

[7] S. K. Jena, S. Chakraverty, Free Vibration Analysis of Single Walled Carbon Nanotube with Exponentially Varying Stiffness, *Curved and Layer. Struct.*, 5, 201-212 (2018).

[8] S, Narendar, *App. Math. Comput.*, 219, 1232-1243 (2012).

[9] A. Belhadj,A. Boukhalfa, and S. A. Bellia, Free vibration analysis of a rotating nanoshaft based SWCNT, *Eur. Phys. J. Plus*, 132. 513 (2017).

[10] J. Shi, Z. Wang, Z. Chen, Concurrence of oscillatory and rotation of the rotors in a thermal nanotube motor, *Computat. Mater.Sci.* 120, 94-98 (2016).

[11] A.C. Eringen, B.S. Kim, RELATION BETWEEN NONLOCAL ELASTICITY AND LATTICE-DYNAMICS, *Cryst. Lattice Defects* **7**, 51-57 (1977).

[12] R. Bellman, B.G. Kashef, J. Casti, Differential quadrature: A technique for the rapid solution of nonlinear partial differential equations, *J. Comput. Phys.* 10, 40 (1972).

[13] C. Shu, B.E. Richards, in Proceedings of 3rd International Conference on Advanced in numerical Methods in Engineering: Theory and Applications, Swansea, Vol. 2 (1990).

[14] S. Chackraverty, L. Behera, Free vibration of non-uniform nanobeams using Rayleigh–Ritz method, *Physica E* 67, 38 (2015).

[15] A. Belhadj,A. Boukhalfa, and S. A. Bellia, Proceedings of the 1st International Conference on Nanomaterials Science and Mechanical Engineering (ICNMSME2019). University of Aveiro, Portugal, July 16-18, (2018).

NANOMATERIALS SCIENCE & ENGINEERING
Vol. 2, No. 3, pp. 113-123 (2020)

RESEARCH ARTICLE

https://doi.org/10.34624/nmse.v2i3.19158

Ni-90 Superalloy Foam Processed by Space-Holder Technique: Microstructural and Mechanical Characterization

Gokhan Timac[1] and H.Ozkan Gulsoy[2, *]

[1] Yalova University, Vocational School of Altınova, Machine and Metal Tech. Dep, 77100 Yalova, Turkey
[2] Marmara University, Technology Faculty, Metallurgy and Materials Eng. Dep., 34722 Istanbul, Turkey
**Corresponding author, e-mail address: ogulsoy@marmara.edu.tr*

Received 7 July 2020; accepted 16 September 2020; published online 22 September 2020

ABSTRACT

In this study, spherical and between 1400 to 1800 µm carbamide particles coated with Ni-90 superalloys powder were used to produce foam by space-holder technique. Foams with porosity between 60%, 70% and 80 vol.% after mixing and compaction the space-holder particles were extracted using hot water leaching over a range of temperatures. The porous green parts were thermally debound to remove the paraffin wax under a pure argon atmosphere then sintered at high vacuum and subsequently heat treatment were performed. The effects of the volume fraction of space-holder particles on density and porosity were investigated. Microstructures were captured using optical and scanning electron microscopy. Also, compression tests were conducted on the sintered, heat treated samples.

1. INTRODUCTION

Traditionally, production of superalloy components begins with the fabrication of large ingots, and these ingots are used in three major production methods to obtain final products. One of these methods are remelting and producing superalloy powders [1]. Rapid solidification associated with powder metallurgy products provides homogeneous microstructures, fine grain structure and enhanced properties. Ni-based superalloys are an unusual group of metallic materials, showing an extraordinary combination of high temperature strength, toughness, and surface stability in corrosive or oxidative environments [1]. Nimonic alloys are one class of Ni-based superalloys developed to give superior creep resistance and are commonly used in wrought form. Nimonic type alloys gain their superior high temperature properties basically from the precipitation of Ni-Al-Ti compounds within a Ni-Cr matrix [2]. These intermetallic precipitates *(γ')* have an ordered cubic L12 structure, and the chemical formulation of these phases is Ni_3(Al, Ti). *(γ')* phase is aluminium rich in most Ni-based superalloys and Ti rich in most Ni-Fe based superalloys [3, 4]. Ni-90 is designed to initially gain high-temperature strength by solid solution hardening brought about by Ni-Cr-Co base alloy strengthened by additions of Ti and Al [2, 3]. However, Ni-90 was designed to gain strength using solid solution initially. It has been developed as an ageing-hardenable creep resisting alloy for service at temperatures up to 920 °C. Given such superior characteristics, they are very important materials for high-temperature applications such as aerospace and power generation industries [5]. Ni-90 superalloy has been developed as an alloy that can harden by precipitation and resist creep under high temperature service conditions. Heat treatment is applied to Ni-90 superalloy to improve its properties or to allow a chemical process to be completed [30]. In particular, the microstructure of Ni-90 superalloys is highly dependent on heat treatment. The selection of the heat treatment to be applied is made according to the desired properties such as

hardness, resistance to breakage and corrosion. [31]. One of the Ni-based superalloys, which has been most successfully applied in the engineering applications, is Ni-90 alloy [6]. Ni-90 superalloy with proper development of the strength to weight ratio could be an alternative to other superalloys and foam materials [7, 8].

Metallic foam materials with controlled porosity are widely used in filtration, wicks, heat pipes, sound attenuation abradable seals, and flow control devices. Even lower densities are being promoted for energy absorption and applications requiring tailored mechanical, thermal, acoustic, and conduction properties [9, 10]. Metallic or ceramic foam materials (open-cell and close-cell) with a volume fraction of pores in the range of 5–80 % can be produced by different techniques (casting, sputter deposition, liquid-state processes – GASAR, and powder metallurgy) [9, 10].

Pore former and powder metallurgy (PM) with space-holder techniques have previously been demonstrated in the fabrication of other metallic and ceramic parts as well as stainless steel and low strength steels [13, 22]. With proper selection of the sintering cycle, the small particles will bond but the large intentional pores will remain. Thus, the process is composed of five sequential steps; (1) mixing of the powder, polymeric molding binder and space-holder particles, (2) compacting or shaping the mixture, for example by axial compression, (3) removing the binder phase and dissolving the space-holder particles without damaging the particle structure usually by a thermal step, (4) sintering the structure to induce strong particle bonding without densification of the pores remaining from the space-holder particles [8] and (5) heat treatment and aging process in sintered parts under suitable thermal cycle conditions. In the speace-holder technique, the initial size and content of the space-holder particles provide the key control over the porosity, pore size, and pore connectivity [11, 12]. Several pore forming agents have been used in the past, including ice, salt, polymers, and volatile compounds such as camphor and ammonium bicarbonate ($(NH_4)HCO_3$) [13, 14]. These have been combined with several metallic powders including aluminum, titanium, stainless steel, and Ni-based superalloys. Both carbamide ($(NH_2)2CO$ also known as urea) and ammonium bicarbonate have been used with thermal extraction by heating below 180 °C; however, there are negative factors from the vapor release from these pore-forming parts [8, 11, 13].

In this work, porous Ni-90 superalloy was produced by the use of a water-soluble space-holder material to sintering. Spherical and specified dimensions carbamide particles were used as the space-holder material. Foams with porosity between 60, 70 and 80 % after mixing and compaction the space holder particles were extracted using hot water leaching over a range of temperatures. The porous green parts were thermally debound to remove the paraffin wax under a pure argon atmosphere then sintered at high vacuum and subsequently heat treatment and aging were performed. The effect of the volume fraction of space-holder particles on density and porosity of the sintered samples was investigated. Microstructures were captured using optical microscopy (OM) and scanning electron microscopy (SEM). Pore size was quantified using image analysis software integral to the SEM. Also, compression tests were conducted on the sintered, heat treatment and aging samples.

2. EXPERIMENTAL PROCEDURE

A schematic illustration of the production processis given in Fig. 1. The binder ingredient for green strength was paraffin wax with a melting range from 123 to 125 °C. It was used at 2 wt.% based on the Ni-90 superalloy mass. While preparing the mixture, Ni-90 superalloy powders and binder components in defined proportions calculated in the recipe were adjusted with a precise balance in determined amounts. Initially, the Ni-90 superalloy powders and paraffin wax were mixed using a double-cone mixer heated to 100 °C to melt the wax. Then carbamide particles is added to the mixture and mixing is done for 30 min was continued. The Ni-90 and carbamide particle ratios were adjusted to give 60, 70 and 80 vol % carbamide particles and paraffin wax in the samples.

Ni-90 superalloy powder used in this study was supplied by Sandvik Osprey Co. and it was produced by high pressure inert gas atomisation. The powder chemical properties were in Table 1. Particle size distributions were determined on

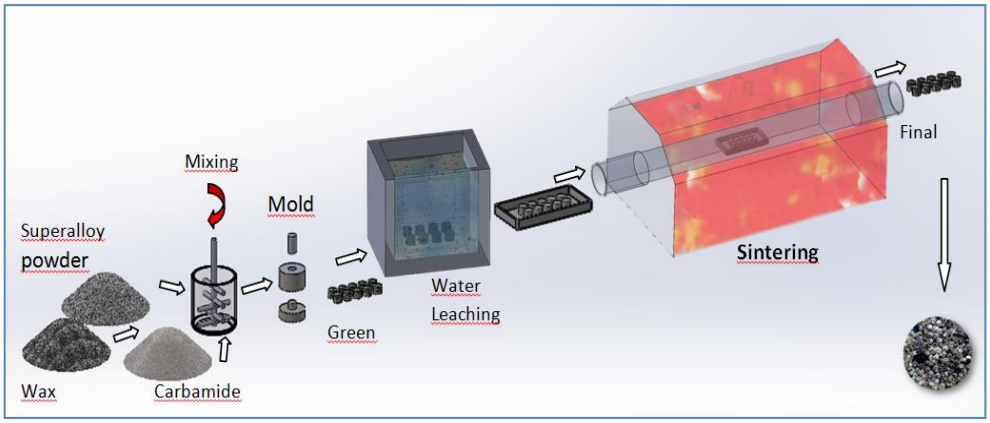

Figure 1. Processing steps of production of porous Ni-90 superalloy samples

Table 1. Chemical composition of Ni-90 superalloy powder

	wt. %								
Material	Ni	Cr	Co	Fe	Al	Ti	C	Si	Mn
Ni-90	57.38	19.50	17.3	0.68	1.02	2.40	0.082	0.94	0.69

Table 2. Physical characteristics of Ni-90 superalloy powder

Item	Ni-90
Vendor	Sandvik Osprey Co.
Shape	Spherical
Tap Density, g/cm^3	5.0
Theoretical density, g/cm^3	8.26
Particle size	
D_{10}	4.1
D_{50}	11.0
D_{90}	24.7

Malvern Master sizer equipment and are shown in Table 2. These indicate that the distribution of particle sizes is suitable for superalloy foam metal with powder metalurgy. The cumulative size distribution at the D_{10}, D_{50}, and D_{90} percent points corresponds to particle sizes of D_{10} : 4.1 μm, D_{50} : 11.0 μm, and D_{90} : 24.7 μm. Carbamide particles were used as space-holder. Carbamide density of 1.34 g/cm^3, melting temperature of 133 °C, and solubility in water at 20 °C of more than 1000 g/L. It was prepared as an irregular particle in a size range from 1400 to 1800 μm. The morphology of the powder and carbamide particle observed using SEM, is given in Fig. 2. The gas atomised Ni-90 superalloy powder and carbamide particle are spherical in shape. The SEM image of the coated carbamide particles with Ni-90 powder is given in Fig. 2.

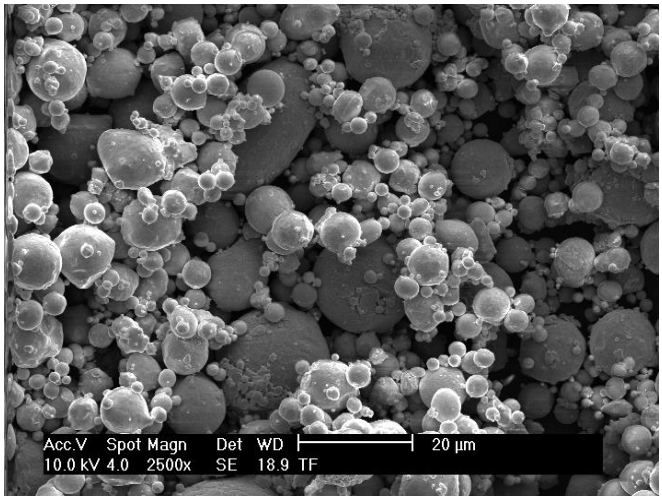

(a)

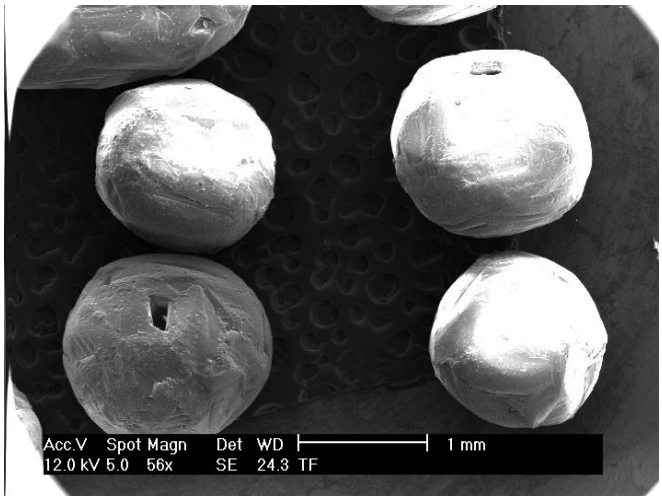

(b)

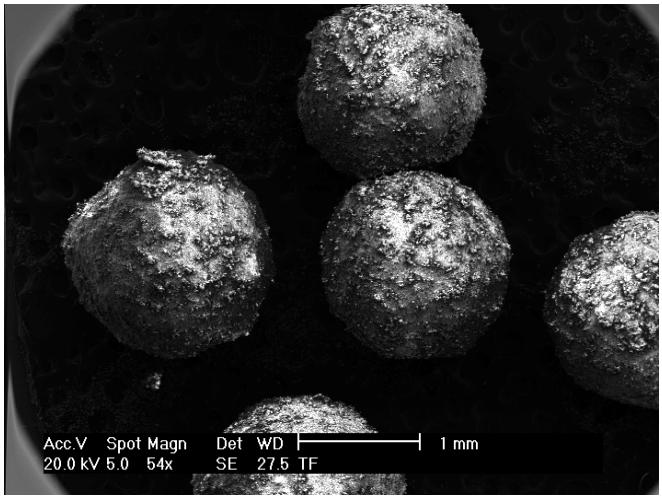

(c)

Figure 2. SEM of (a) Ni-90 superalloy powder, (b) carbamide particles and (c) coated carbamide particles with Ni-90 superalloy powder

powders was performed in a Turbula mixer for 1 h. The mixtures were compacted at 100 MPa into cylinders with a diameter of 19 mm and height of 20 mm. The green samples which foams with porosity between 60, 70 and 80 % were held at 30 and 40 °C for times ranging from 1 to 6 h in distilled water for extracted using hot water leaching of carbamide particles. The paraffin wax was thermally removed as a part of the sintering cycle, which consisted of heating step-by-step at 1 °C/min to 600 °C with a 6 h hold, followed by heating at 5 °C/min to 900 °C for 1 h in high purity argon to pre-sinter samples. This was performed subsequent final sintering relied on a heating rate of 10 °C min^{-1} to 1300 °C for 1 h under vacuum (10^{-3} Pa). In this study, standards and Precision Castparts Corp. (Special Metals), the most suitable temperature and time for the aging and heat treatment of Ni-90 materials have been determined. The sintered samples were solution treated at 1080 °C for an hour as specified in the literature for alloy Ni-90 [15] and then cooled down in the water. The solution treated samples were aged at 705 °C for 16 h.

The density was calculated by dividing the mass of the compact by its volume, which was calculated from physical dimensions. Samples were mounted in epoxy and polished as standard metallographic procedures. Microstructures were obtained via OM (Olympus BX50) and SEM (FEI-Srion) after etching. Compression tests were performed at a crosshead speed of 1 mm/min. (Instron-8802 universal materials testing system). At least three specimens were tested under the same conditions to assess repeatability, and average values were used. After, the effect of the aging treatment was followed by hardness and X-ray diffraction (XRD) measurements. XRD analyses of the starting powder and the sintered and aged parts were performed out on a LabX- XRD 6100 device using Cu X-ray tube (λ=1.5405) and with a 0.02/0.4 s. scanning step. Microhardness measurements of the sintered materials were performed on the $HV_{0,2}$ scale (Shimadzu).

3. RESULTS AND DİSCUSSİON

Ni-90 superalloy samples with porosity ranging between 60, 70, and 80 % were successfully produced temperature (slightly low for this material and particle size), the sintered density was 8.26 g/cm^3 (97% relative density). Sintered densities of 3.3 and 2.5 g/cm^3 (39,9% and 30,2% relative density) were obtained with 60 and 80 % carbamide particles additions, respectively. Fig. 3. shows the sintered and heat treated samples having 60, 70, and 80 % porosity. OM micrographs of the cell wall of foam are also shown. In all samples, the morphology of the pores was similar to that of the carbamide powder particles. The foams were observed to contain mainly two types of pores: macropores obtained as a result of carbamide space-holder and micropores on cell-

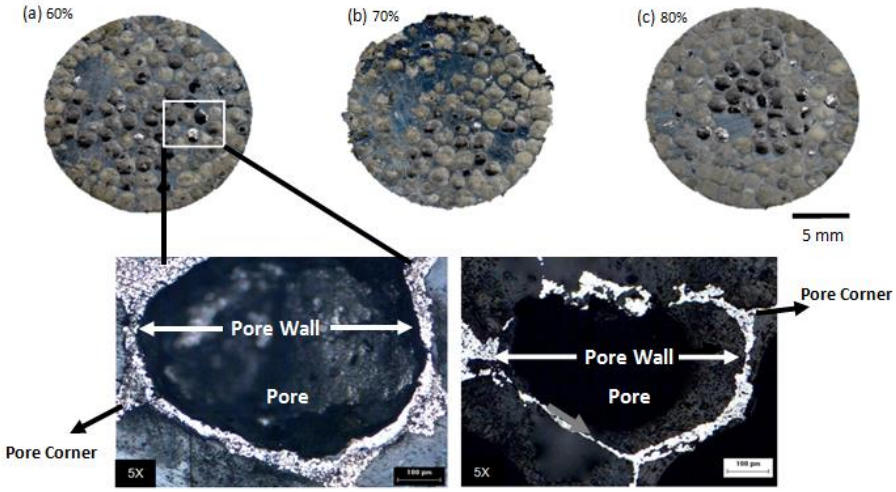

Figure 3. Macroscopic morphology of sintered Ni-90 superalloy samples from surface (a) sintered and aged for 60 vol. % (b) sintered and aged for 70 vol. % (c) sintered and aged for 80 vol. %

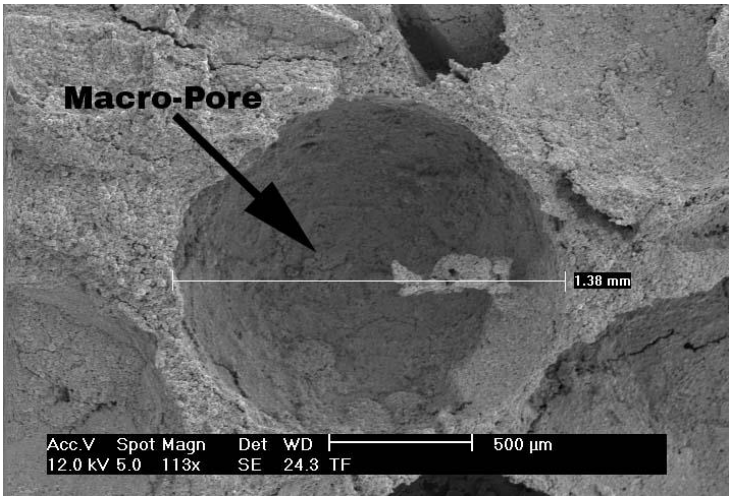

(a)

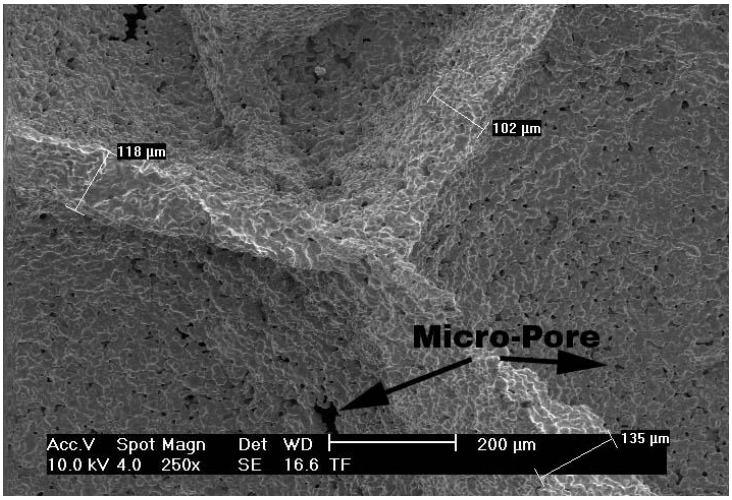

(b)

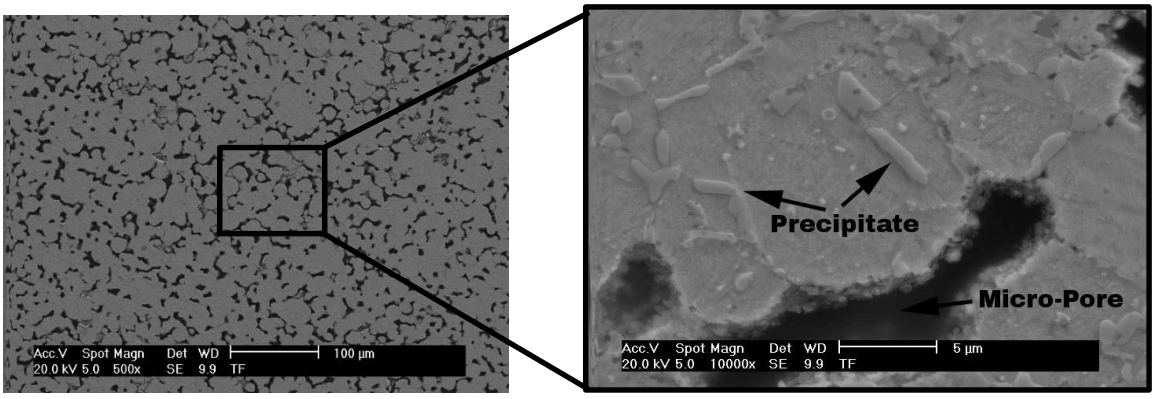

(c)

Figure 4. SEM micrographs of Ni-90 superalloy foam for 80 %, (a) heat treatment macro-pore, (b) aged micro-pore and (c) aged microstructure samples

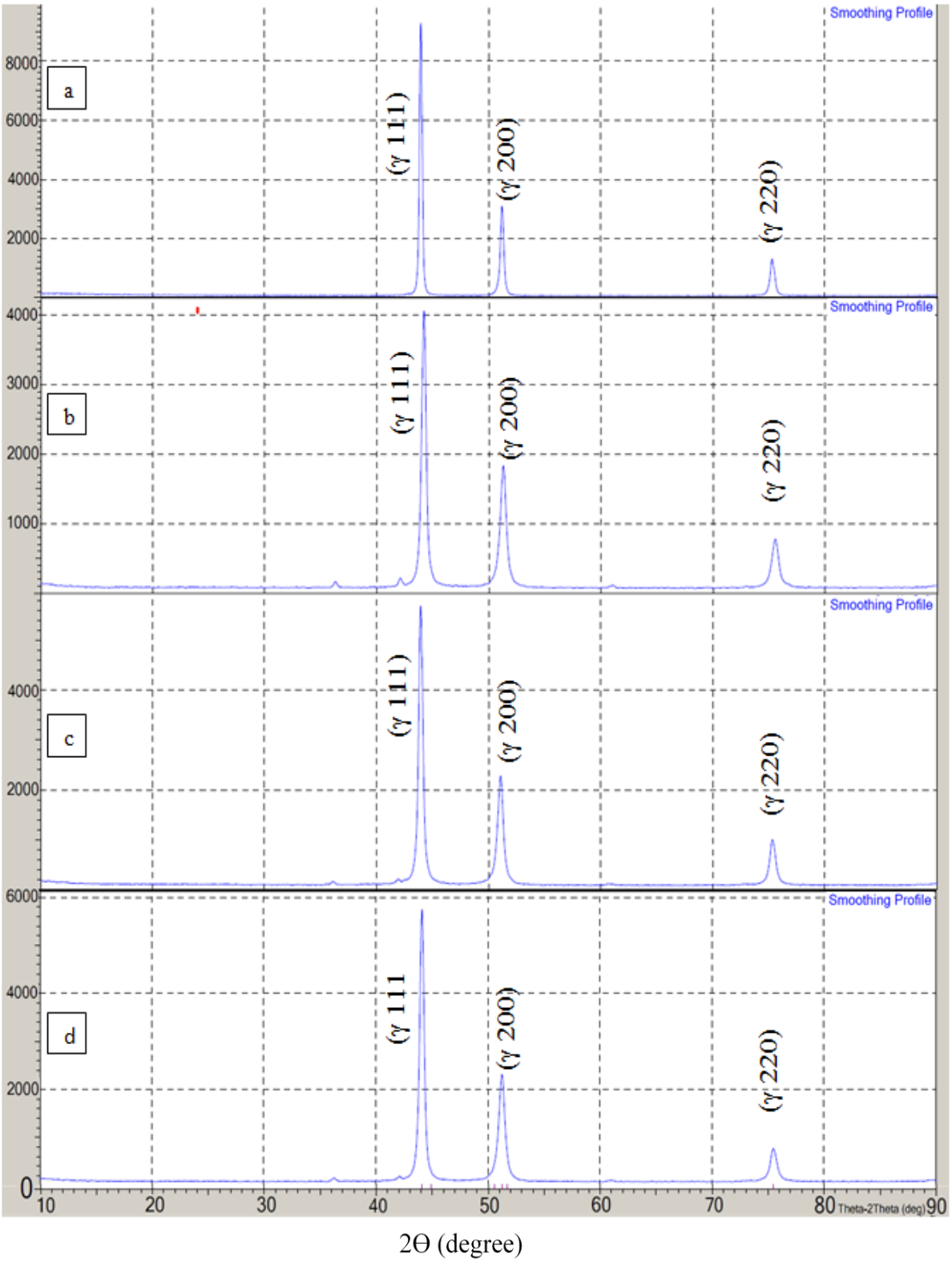

Figure 5. XRD diffraction patterns of (a) Ni-90 superalloy powder, (b) sintered, (c) solutioned and (d) aged samples

Ni-90 superalloy foam. By adjusting some space-holder particles, the porosity of the resulting Ni-90 foam can be altered. Macropores become directly connected above a porosity of 60 %, which may vary with the size of the space-holder particles and the powders constituting the cell walls [12, 16].

Fig. 4a shows the structure of a typical cell and the cell walls of Ni-90 superalloy foam produced by space-holder technique, which has a carbamide of 80 vol.%. The interconnecting cell channels are also clearly shown. Fig. 4b shows the bonding region between Ni-90 particles in the sample, indicating that strong bonds have formed between the particles. As can be seen in Fig. 4b, the microporosities existed in the sample. The microporosity in the sintered sample should be kept as low as possible if a high-strength porous metal solid were desired. SEM analysis was performed on heat-treated Ni-90 foams, as shown in Figure 4c. The basic phase that provides an increase in strength in most Ni-based superalloy which can be hardened by precipitation is *γ′* phase. Precipitation of the *γ′* phase in the matrix containing high Ni results in a significant increase in hardness and strength. The reason for this increase is thought to be the formation of γ ' [Ni3 (Al, Ti)] intermetallic precipitate and the smaller volume of γ ' phase formed and homogeneous distribution for the whole structure during the aging time by heat treatment. This unique intermetallic phase is FCC-like, similar to the gamma matrix, and the lattice constant exhibits 1% or less incompatibility with the gamma matrix [17]. The *γ′* phase precipitation in the supersaturated matrix provides a significant increase in strength. Since the strength of the material will increase with the amount of *γ′* phase it contains, the volume ratio of the collapsed *γ′* phase is also important. The amount of *γ′* phase formed depends on the content of the hardening alloy element. These elements are strong *γ′* forming Al, Ti, Nb and Ta elements [17].

In order to understand whether there is phase change in microstructure due to sintering, cavity forming, heat treatment and aging processes the XRD analysis was performed. XRD analysis was performed on the following samples; prealloyed Ni-90 starting powder, sintered Ni-90 foam metal samples with 60-70-80 % porosity, Ni-90 sample sintered without porosity, heat treated Ni-90 foam metal samples with 60-70-80 % porosity and aged Ni-90 foam metal samples with 60-70-80 % porosity. As a result of the XRD analysis, it was observed that the patterns obtained from all samples were almost the same. Some of their diffraction patterns are shown in Fig. 5. Carbide and *γ′* phase precipitates should be formed in the microstructure since the samples are left for cooling at 1000 °C/min without removing the tube from the furnace after sintering is performed for 1 hour at 1300 °C. However, the carbides (which are thought to be formed) and the intermetallic precipitates (which bring out the strengthening properties) are too small to be captured by XRD analysis. Carbides and especially intermetallic precipitates, which are the purpose of the aging treatment, cannot be detected by XRD analysis due to their low concentrations. However, it was indicated that the changes observed in the XRD patterns of the gamma matrix could be used to determine indirectly the presence of precipitates [18].

Fig. 6a. shows the compressive stress-strain curves of baseline and porous Ni-90 sintered samples with different fractions of carbamide. When the non-porous sample reaches 905 MPa stress (strain 25 %), the corresponding stress for carbamide-added samples at 60, 70, and 80 % are 52, 100.8, and 125.6 MPa, respectively. Fig. 6b. shows the compressive stress-strain curves of baseline and porous Ni-90 sintered and aged samples with different fractions of carbamide. When the non-porous sample reaches 905 MPa stress (strain 25%), the corresponding stress values for carbamide added samples at 60, 70, and 80 % are 24, 89.2, and 122.5 MPa, respectively. Fig. 6. shows a common stress–strain behavior characterized by three distinct regions (i.e., stress rising linearly with strain at low stresses (elastic deformation), followed by a strong plastic yielding for strains, and then a progressive densification regime where the cell walls come in contact one with another, causing an abrupt rise in the flow stress [7, 9, 10, 16, 19-22]. Once the cell edges collapse at the yield point, the collapsed edges have little ability to bear the load and bend easily. The deformation mode, resulting from the repeatable failure of the pore layers, gives rise to the uneven character of the stress–strain curve. The plateau region of the foam material subjected to the compression force is associated with the

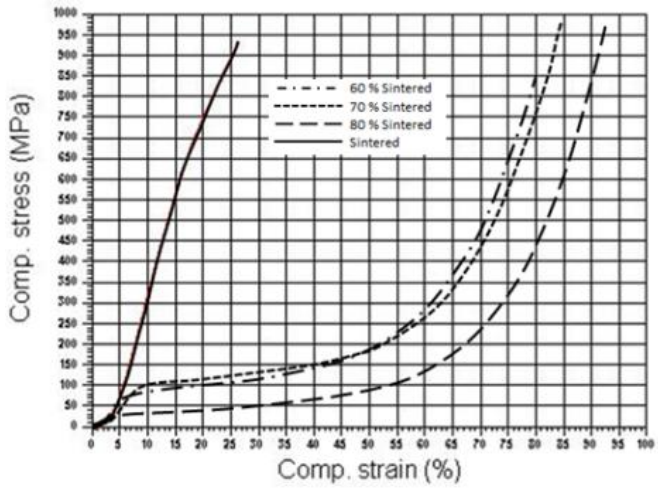

(a)

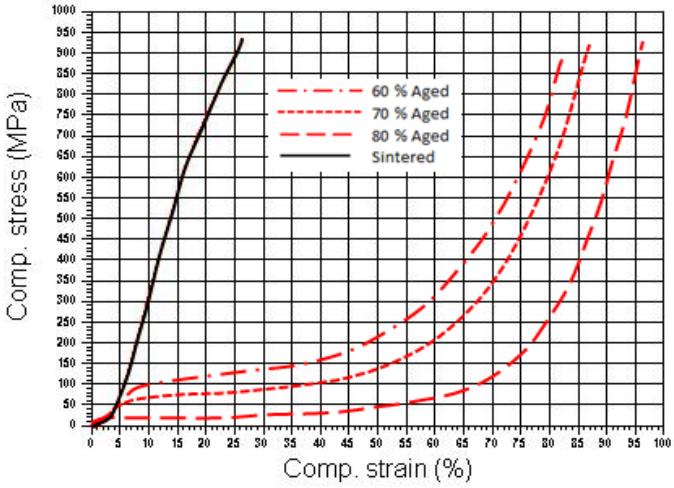

(b)

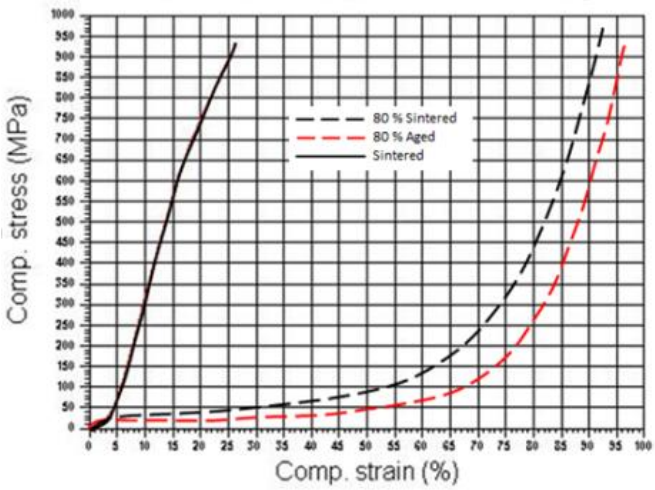

(c)

Figure 6. Compressive stress- strain curves of porous Ni-90 superalloy foam samples with 60 – 80 % carbamide, (a) sintered samples (b) sintered and aged samples (c) sintered and aged for 80 vol. %

where the stress is constant, metallic porous materials have the ability to absorb energy without exceeding a certain stress limit [32, 33]. At the end of the plateau region, stress starts to increase since the pores have flattened and the material attains bulk-like properties. The plateau region has vital importance for the applications requiring energy absorption capability. Compression tests of the porous samples showed that the compressive strength values decreased and length of the plateau region increased with increasing porosity [9, 19, 23–27]. Fig. 6c. shows a comparison of sintered and aged samples for 80 % porosity. When compared the sintered and aged samples, strain values of the aged samples are higher than those of sintered samples. Depending on the aging process, elongation of the samples was developed. Since the carbamide particles are contained in the structure between 60,70 and 80% by volume and emerge as a void at the end of the process, the sintered density decreased. This increased the tension of porous samples. The strength of the samples increased as the porosity decreased.

5. CONCLUSION

In this study, defined sizes of spherical carbamide particles coated with Ni-90 superalloys powder were used to produce foam in powder metallurgy using the space-holder technique. Then sintered at high vacuum and subsequently heat treatment and aging were performed. Experimental results show that a carbamide pore former, nearly 100-fold larger than the Ni-90 superalloy particles, provides a means to retain large pores in the sintered part. By extraction of the carbamide by water leaching after compaction, medium density Ni-90 superalloy foams are realized by a traditional powder metallurgy route. The green compact had sufficient strength for handling after water leaching at sintering stages. Metallographic studies revealed a relatively uniform distribution in the sintered structure when the two-dimensional visual structures of the top, bottom and cut samples of samples with 60, 70 and 80% porosity were examined. Large numbers of micropores formed in the cell-walls due to insufficient solid-state sintering. No distortion or other visible reduction in part quality or surface finish was observed at 1300 °C for 1h under vacuum and for aged 705 °C. When the morphology images are examined, it is seen that the pores are mostly between the grains and there are almost no pores trapped in the grain. It has been observed that the grain size of the material has slightly increased with the sintering process. By comparing the physical and mechanical properties of the samples with the homogeneous porous structure, sintered density decreased, porosity increase with a fraction of space-holder particles increment was observed. Compression tests have shown that heat treatment increases the strength values of the Ni- 90 alloy. As a result of XRD analysis, no pike other than gamma matrix peaks was found in the patterns of both the starting powder, the pore-free sintered and the aged sample. It is thought that after sintering and aging, carbide and γ 'phase precipitates should be formed in the microstructure. However, it is thought that the carbides thought to be formed and especially the intermetallic precipitates, which are the purpose of the aging process, are in such small quantities that cannot be detected by XRD analysis. Comparing the XRD patterns, the decrease in the intensity of the gamma matrix peaks in the sintered sample compared to the starting powder indicates that after the sintering process, a large amount of precipitate phase was formed in the material.

ACKNOWLEDGEMENTS

This study was supported by the Scientific Research Projects Coordination Unit of Marmara University, Project number FEN-C-DRP-090512-0172. The authors are grateful to Sandvik Osprey Co. for their financial support and the provision of laboratory facilities.

REFERENCES

[1] T.M. Pollock, S. Tin, *J. Propul. Power* **22**, 361–374 (2006).
[2] W. Betteridge, (1959) The Nimonic alloys, Edward Arnold Ltd. London.
[3] E.W. Ross, C.T. Sims, (1987) Superalloys-II., John Wiley & Sons. New York.
[4] E.F. Bradley, (1988) Superalloys: a technical guide, ASM International. Metals Park, OH.
[5] S.L. Semiatin, K.E. McClary, A. D. Rollett, C. G. Roberts, E. J. Payton, F. Zhang & T. P. Gabb, *Metall. Mater. Trans. A*, **43,** 1649-1660 (2012).
[6] M.J. Cieslak, (1991) Proceedings of the International Symposium on the Metallurgy and Applications of

Superalloys 90, 625 and Various Derivatives. TMS, USA.
[7] J. Kovacik, J. Jerz, N. Minarikova, L. Marsavina, E. Linul, *Frattura ed Integrita Strutturale* **36**, 5563 (2016).
[8] H.O. Gulsoy, R.M. German, *Pow. Metall.* **51**, 350-353 (2008).
[9] Eds. M.F. Ashby, A.G. Evans, N.A. Fleck, L.J. Gibson, J.W. Hutchinson, H.N.G. Wadley, (2000) Metal Foams: A, Elsevier Inc.
[10] A.E. Simone, L.J. Gibson, *Acta Mater.* **44**, 1437-1450 (1996).
[11] B. Jiang, N.Q.Zhao, C.S. Shi, J.J. Li, *Scripta Mater.* **53**, 781-785, (2005).
[12] D.J. Sypeck, P.A. Parrish, H.N.G. Hayden, (1998) Materials Research Society Symposium Proceedings. 205-219., MRS, USA.
[13] Y.Y. Zhao, D.X. Sun, *Scripta Mater.* **44**, 105-110 (2001).
[14] Martin Bram, Cornelia Stiller, Hans Peter Buchkremer, Detlev Stöver, Hartmut Baur, *Adv. Eng. Mater.* 2, 196-199 (2000).
[15] O. Ozgur, H.O. Gulsoy, R.Yilmaz, F. Findik, *J. Alloys and Comp.* **576**, 140-155 (2013).
[16] N. Michailidis, F. Stergioudi, A.Tsouknidas, E. Pavlidou, *Mater. Sci. Eng. A*, **528**, 1662-1670 (2011).
[17] G.L. Erickson, (2005) Polycrystalline Cast Superalloys. In Asm Handbook: Properties And Selection: Irons, Steels, And High Performance Alloys, 1:1532-1550, ASM, USA.
[18] R.B. Li, M. Yao, W.C. Liu, X.C. He, *Script. Mater.* **46**, 635–638 (2002).
[19] J. Banhart, *Prog. Mater. Sci.* **46**, 559-570 (2001).
[20] J. Kovacik, F. Simancik, *Kovove Mater.* 42, 79-90 (2004).
[21] D.C. Dunand, *Adv. Eng. Mater.* 6, 369-375 (2004).
[22] H.I. Bakan, *Scripta Mater.* 55, 203-208 (2006).
[23] N. Bekoz, E. Oktay, *Mater. Process. Tech.* **212**, 2109-2116 (2012).
[24] M. Kohl, T. Habijan, M. Bram, H.P. Buchkremer, D. Stover, M. Koller, *Adv. Eng. Mater.* **11**, 959-968 (2009).
[25] A. Bansiddhi, D.C. Dunand, *Mater. Eng. and Perf.* **20**, 511-516 (2011).
[26] I. Mutlu, E. Oktay, *Mater. Sci. Eng. C*, **33**, 1125-1131 (2013).
[27] I. Mutlu, E. Oktay, *Mater. Des.* **44**, 274-282 (2013).
[28] R.J. Mitchell, C.M.F. Rae, S. Tin, *Material Science And Technology* 21, 125-132 (2005).
[29] M. Sundararaman, *Mineral Processing and Extractive Metallurgy Review* 22, 681-700 (2002).
[30] Mj. Donachie, Sj. Donachie, (2002) Selection Of Superalloys For Design. In Handbook Of Material Selection, John Wiley & Sons, Inc. B, 10: 293-334.
[31] M. Retima, S. Bouyegh, H. Chadli, Effect Of The Heat Treatment On The Microstructural Evolution Of The Nickel Based Superalloy. *Metalurgija-Mjom*, **17(2)**, 71-77 (2011).
[32] Cs. Kadar, P. Keneseı, J. Lendvaı, Zs. Rajkovıts, Energy absorption properties of metal foams, VI. évfolyam 1. szám, 6. (2005).
[33] C.Wang, R. Li, Effect Of Double Aging Treatment On Structure In Inconel 718 Alloy, *Journal of Materials Science*, **39**, 2593 – 2595. (2004).

NANOMATERIALS SCIENCE & ENGINEERING
Vol. 2, No. 3, pp. 124-134 (2020)

RESEARCH ARTICLE

https://doi.org/10.34624/nmse.v2i3.19533

Comparison between the performances of different boring bars in the internal turning of long overhangs

Wallyson Thomas*, Zsombor Fülop, Attila Szilágyi

István Sályi Doctoral School of Mechanical Engineering Sciences – University of Miskolc – Egyetemváros, 3515, Miskolc, Hungary
**Corresponding author, e-mail address: szmwally@uni-miskolc.hu*

Received 22 July 2020; accepted 16 September 2020; published online 22 September 2020

ABSTRACT

Impact dampers are mainly used in the metal-mechanical industry in operations that generate too much vibration in the machining system. Internal turning processes become unstable during the machining of deep holes, in which the tool holder is used with long overhangs (high length-to-diameter ratios). The devices coupled with active dampers, are expensive and require the use of advanced electronics. On the other hand, passive impact dampers (PID – Particle Impact Dampers) are cheaper alternatives that are easier to adapt to the machine's fixation system, once that in this last case, a cavity filled with particles is simply added to the structure of the tool holder. The cavity dimensions and the diameter of the spheres are pre-determined. Thus, when passive dampers are employed during the machining process, the vibration is transferred from the tip of the tool to the structure of the boring bar, where it is absorbed by the fixation system. This work proposes to compare the behaviours of a conventional solid boring bar and of a boring bar with a passive impact damper in turning while using the highest possible L/D (length-to-diameter ratio) of the tool and an Easy Fix fixation system (also called: Split Bushing Holding System). It is also intended to optimize the impact absorption parameters, as the filling percentage of the cavity and the diameter of the spheres. The test specimens were made of hardened material and machined in a Computer Numerical Control (CNC) lathe. The laboratory tests showed that when the cavity of the boring bar is totally filled with minimally spaced spheres of the largest diameter, the gain in absorption allowed of obtaining, with an L/D equal to 6, the same surface roughness obtained when using the solid boring bar with an L/D equal to 3.4. The use of the passive particle impact damper resulted in, therefore, increased static stiffness and reduced deflexion of the tool.

1. INTRODUCTION

One way to attenuate internal turning vibration is to reduce the cutting forces by changing the machining parameters (decreasing depth of cut, cutting speed, and feed rate). These changes reduce productivity dramatically. Another way is to use active or passive dampers attached to the boring bar to avoid or minimize vibrations [1].

That vibrations might be quite undesirable, as they not only compromise the performance of components but may also cause damage beyond repair. Therefore, vibration control techniques are important in the study of vibrations. The function of dampers in vibratory systems is to dissipate the energy generated by the vibratory movement, thus decreasing the vibration amplitude. The particle impact damper is a device that increases the dampening capacity of the structure by inserting particles within a cavity in a vibrating structure [2].

Picture a structure that vibrates over a certain time period. In a given instant, this structure contains a certain amount of kinetic energy and a certain amount of deformation or potential energy; the kinetic energy is associated with its mass and the deformation energy is associated with its stiffness. Besides that, a real structure, when deformed, dissipates part of the energy. This

energy dissipation, called damping, is a conversion of mechanical energy into heat energy [3].

The principle of operation of a particle damper is based on the energy dissipation through multiple inelastic collisions and the friction among particles and between the particles and the cavity wall. The resulting system is non-linear, as its vibratory response is mostly dependent on the excitation amplitude. The damping capacity depends on the level of acceleration undergone by the cavity. There are many parameters that affect the performance of a particle damper [4]. The predominance of one dampening mechanism or another is related to the dynamic characteristics of the machining process, as, unfortunately, the transference of linear moment that happens during the collisions is insufficient to dissipate most of the vibration energy, while the friction is efficient to dissipate energy only at high vibration frequencies and might even hinder the system performance at low frequencies [5].

With the modern technology in viscoelastic materials, vibration neutralizers became easy to both produce and apply to almost any structure, no matter how complex it is [6]. An example of this are Sandvik's anti-vibration boring bar (Silent Tools), that have pre-tuning system for the frequency, related to the tool overhang required by the fixation system. Its efficiency may achieve an L/D (length-to-diameter ratio) of 10 for steel tools and of 14 for cemented carbide tools. Boring bar made of materials with a high elastic modulus, as cemented carbides, are frequently used as absorbing elements, have greater dynamic stiffness and allow of performing stable cuts with L/D up to 7 [7].

The dampening effect generated by an impact damper happens as part of the energy of the vibrating structure is transferred to the particles, or spheres, that collide against each other. Traditional absorbers, such as the ones made of viscoelastic materials (Silent Tool), convert elastic deformation energy into heat and noise. One should add that, similarly to impact dampers, traditional absorbers have a series of applications, but are efficient only in certain conditions, as they lose much of their efficiency in environments where the temperatures are too high or too low, degrading more rapidly than impact dampers [8,9]. The latter, on the other hand, may be used in cutting tools, television towers, turbine blades, axes, panels, and others [10]; as they low cost and simple to build, of easy maintenance and may work for large frequency spectrums [11]. Besides that, an important advantage is that their efficiency (damping capacity) is not affected by temperature. Additionally, their implementation is simple and does not damage the surface of the machined part. Finally, they're tools to control the noise and the vibration that result from the interaction between the tool and the machined part. One of the disadvantages of impact dampers is their remarkable non-linearity, which implies difficulties in adjusting the absorption parameters – such as the stiffness and the restitution coefficient of the boring bar, and the space between the spheres and the cavity – at each time the mass of the system changes [12]. Also, it should be kept in mind that the particle impact damper is efficient at only a specific frequency range. The challenge, therefore, is to find that frequency range of greater efficiency. Hence, it is important to notice that, because of that limitation, this type of damper is rarely used in applications where the operating conditions change [13].

2. LITERATURE REVIEW

The efficient use of the particle impact damper requires a careful configuration of its parameters – such as the diameter, density and dimensions of the particles, the shape of the cavity and the type of excitation (vibration) from the primary system. Other important factors to configure the damping system are the force and frequency of vibration, the masses of the particles and of the structure, the stiffness and the damping capacity of the structure, the space between the particles and the main system, the natural frequency of the main system, the initial displacement and the restitution coefficient [10]. Hence, the study of the damping mechanism is quite complex [12,13].

In dampers with micro particles whose cavity in the boring bar is small, the damping action takes place as the particles get stacked in layers – this happens in such a way that the movement of the inferior layers is minimized and a more intense movement is created in the upper layers. This results in reduced kinetic energy transference and an effective decrease in the damping capacity. As for the cavities in average size boring bar, the

damping system is more sensitive to the particle size – if the particle size is decreased, the vibration is not decreased, as it depends on the gap between the particles and the cavity. As for large cavities, any type of particle may be used, as the energy dissipation by the collisions among the particles in the cavity is inefficient. When large spheres are used, the directions of the impact against the cavity wall and the direction of excitation are practically parallel, being that this impact energy is low compared to the mass of the whole system. It is possible to say that, if the diameter of the spheres is smaller than 2 times the diameter of the cavity, no collision between the spheres and the cavity walls might happen. This may be the case when the direction of the excitation is perpendicular to the wall, in such a way that the spheres collide sporadically against the upper and lower walls of the cavity [15, 16].

Olson and Drake (1999) performed experiments using a PID (Particle Impact Damping) system which had a medium sized cavity, in a boring bar fixed to a laboratory device and excited in different frequencies by an electrodynamic shaker. It was concluded that the spheres move in only one direction and do not collide in other directions. As the spacing between the spheres and the cavity is small, or pre-determined, the spheres collide in a relatively orderly manner and in only one direction, which improves their dampening capacity, as the impact of the collision is concentrated in a small region. This avoids the energy waste that would happen if the spheres collided against various regions, with linear moments of multiple directions. Such concentration of the collision force enhances the system efficiency in dissipating energy [8].

If some variables are held constant – such as the frequency of excitation, the diameter of the spheres and the amount of spheres in the cavity, among other factors – and only the spacing between the spheres (gap) is modified, the absorption efficiency of the system, as well as the damping factor, increase dramatically. The work of Friend and Kinra (2000) shows the possibility of estimating theoretically this gab by using some equations, as well as through FEA (Finite Element Analysis) [17]. These authors also relate the gap and the decay rate of the vibration amplitude of the structure. Greater gaps imply greater rates, whereas smaller gaps imply reduced rates, albeit a greater number of impacts occur in the last case – this shows that the number of impacts is not the main factor that affects the energy dissipation.

The friction, among other factor, reduces the speed of the moving particles. The material of the sphere, the friction coefficient between the spheres, the amount of particles, the number of particles and the volume fraction of the cavity occupied by the particles affect the friction phenomena within the cavity [12]. Zhiwei and Wang (2003) estimated that the maximum volume fraction that may be occupied by spheres in a cavity is would correspond to values between 52 and 74 %. Those values are, respectively, equivalent to the maximum and minimum atomic packing factors found in cubic crystalline structures. The minimum and maximum spacing between the spheres may be determined, which allows of previewing some parameters, such as the number of sphere layers, the size of the spheres, the cavity dimensions and the volume occupied by the spheres [18].

3. MATERIALS AND METHODS

The main concern of this work consists in the comparative analysis of the tool vibration in the internal turning of hardened materials while using a conventional boring bar and a boring bar containing a passive impact damper.

Two 20 mm diameter boring bars (ISO code A20S-SCLCR 09-R 1M 0866943) were chosen – they were kindly supplied by Sandvik Coromant. The boring bar with a passive impact damper has cavity (hole in the axial direction) to accommodate the steel spheres, and a pre-adjustment system, as illustrated in figures 1 (a) and (b).

One of the steel boring bars was modified to accommodate the particle impact damper. The tool was drilled in its longitudinal direction and a thread was made in one of its extremities, in such a way as to create a closed compartment. The hole had a 10.5 mm diameter and a 160 mm length, as depicted in figure 1 (b). This cavity was then filled with steel spheres. The spheres used in the experiments were of AISI 52100 chrome steel and had diameters of 9, 10 and 10.32 mm. They were grinded, polished, free of surface defects and had a hardness of 60 - 66 HRC.

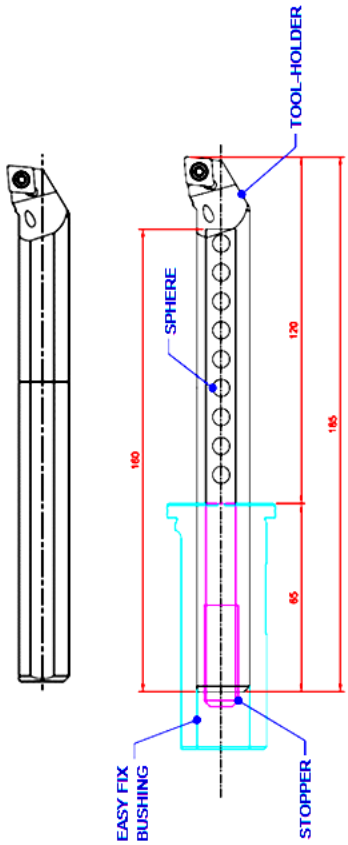

(a) (b)

Figure 1. Conventional boring bar (a) and boring bar with cavity (b).

As for the tool insert, an adequate insert for finishing operations on smooth surfaces of hardened steels was chosen. It was composed of CBN it's ISO code is CCGW09T308S01020F 7015 (grade ISO H10). The advantage of the chosen tool insert, when compared to others with a greater CBN content, is its chemical stability in relation to iron. Besides, its toughness is enough to preserve its cutting edge, even tough it is reduced when compared to other inserts with a greater CBN content.

The FRFs (Frequency Response Function) of the tool holders were obtained for different overhangs (length of the tool holder that protrudes from the turret) through impact tests (hammer impact test). In each test, the boring bar was fixed to the turret of the machine tool used in the turning tests, as it is further described, with the desired L/D. An accelerometer was installed on the boring bar, which was then hit with an instrumented impact hammer. Each impact was considered a measurement – 5 measurements were done for each L/D and each one of the boring bars used. In the data acquisition, a frequency range of 0 to 10000 Hz was used, with a resolution of 1 Hz, the smallest possible in data acquisition software used. For each test, the software calculated an average of the 5 measurements that were executed and made the results available. Boring bar overhangs corresponding to length-over-diameter ratios (L/D) greater than 3 were experimentally evaluated, as smaller ratios do not yield interesting results for this research, as it has also been evaluated by Hoshi (1990) [19, 20].

The 4340 steel used in the fabrication of the test specimens is a widely employed material in the metal mechanical industry. It presents high hardenability, bad weldability and reasonable machinability, as well as a good resistance to torsion and fatigue –its hardness after quenching varies from 54 to 59 HRC. Its chemical composition is presented in Table 1.

The dimensions of the test specimens are shown in figure 2, where the 30 mm hole that was machined during the tests is shown. The tool swept its surface several times as it was machined, in

Table 1. Chemical composition of the material of the test specimens (% wt).

C	Si	Mn	Cr	Ni	Mo	V
0,4	0,25	0,65	0,76	1,68	0,23	0,003

Ti	Al	Cu	P	S	Ceq
0,002	0,015	0,11	0,018	0,02	0,83

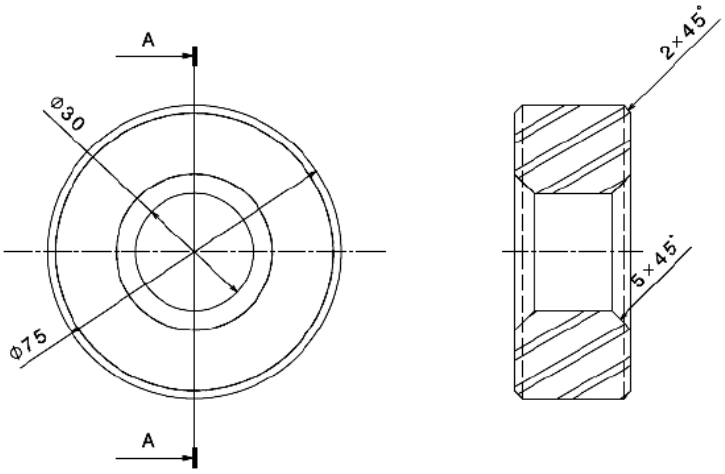

Figure 2. Dimensions of the test specimen, in millimetres [mm].

such a way that the hole's diameter grew during the test. When the diameter reached a limit dimension of 50 mm, the test specimen was discarded, in order to make sure that there would be no substantial hardness variation on the machined surface.

After testing the conventional boring bar, tests with the boring bar containing a cavity were done. By using the conditions described in table 2, it was searched to obtain the best performance of this last tool, that is, a machining process with no chatter and an average roughness of the machine surface lower than to 0.8 µm. The spheres were employed with the aim of increasing the system's stiffness and damping the machining vibrations. Hence, the following procedure was adopted: the boring bar was fixed to the turret with one of the L/D in table 2, and its cavity was filled with spheres correspondingly. The boring bar was also tested with an empty cavity.

After each test, the FRF of the bar configuration was obtained as previously described. Then, to

(a) (b)

Figure 3. Surface generated by a (a) stable cut and (b) unstable cut [5].

Table 2. Set up conditions of the tool with a cavity.

TOOL OVERHANG (L) [mm]	L/D	Ø SPHERE [mm]	VOLUME FRACTION (VF) [%]
120	6	10.32	70%
		10	60%
		9	50%
110	5.5	10.32	70%
		10	60%
		9	50%
100	5	10.32	70%
		10	60%
		9	50%
90	4.5	10.32	70%
		10	60%
		9	50%
80	4	10.32	70%
		10	60%
		9	50%
70	3.5	10.32	70%
		10	60%
		9	50%
68	3.4	10.32	70%
		10	60%
		9	50%

measure its radial acceleration, an accelerometer was fixed on the boring bar and a 15 mm length was machined in the 30 mm hole in the test specimen. Next, the roughness of the machined surface was measured as the test specimen was still fixed in the lathe. The roughnesses of the machined surfaces were measured with a portable Mitutoyo roughness tester (SJ-201P model) connected to a computer. The software SurfTest, which was installed in this computer, was used to obtain the data and the surface roughness profiles.

It is important to define some expressions employed in this work, which are:

- Stable cut: internal turning operation where the vibrations present acceleration signals inferior to 100 m/s2; and which yields a surface whose roughness is less than 0.8 µm and that is free from chatter marks, as shown in figure 3 (a);
- Unstable cut: the surface roughness of the machined surface and the acceleration in turning exceed the values cited above as acceptable for a stable cut. A surface as the one shown in figure 3(b) may be generated;
- Conventional boring bar: boring bar with no cavity, spheres, or threaded bar (stopper), as illustrated in figure 3 (a);
- Boring bar with cavity: boring bar with a longitudinal inner hole, filled or not with spheres to damp vibration, as illustrated in figure 3 (b). One may notice that the cavity should be made as close as possible to the tip of the tool, where the greatest deflexions occur.

4. RESULTS

At first, an optimal configuration of the boring bar filled with spheres was searched, aiming a stable cut, that is, with no chatter or noise. Thus, the average roughnesses (Ra) of the surfaces machined with different L/D, as well as the average accelerations (RMS), were compared. Figure 4 (a) presents the surface roughnesses values obtained after the internal turning operations performed with boring bar filled with 9, 10 and 10.32 mm diameter spheres. For all L/D tested, the roughness values are close when 9 and 10 mm spheres are used. It

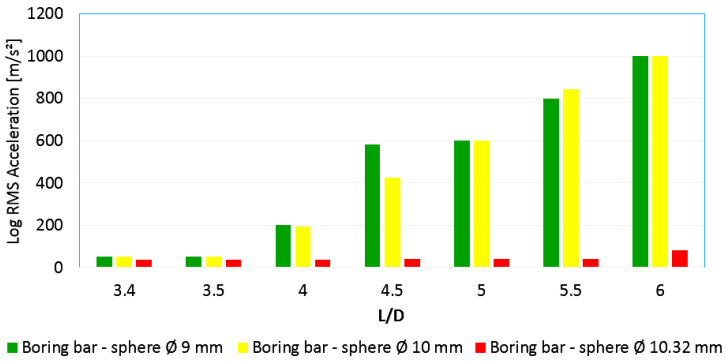

(a)

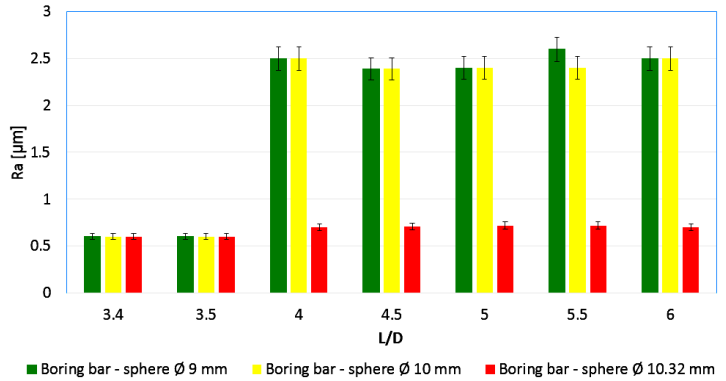

(b)

Figure 4. (a) Acceleration values and (b) average surface roughness (Ra) obtained with the too-holders filled with Ø 9, Ø 10 and Ø 10.32 mm diameter steel spheres.

may be seen, too, that for boring bar filled with 9 and 10 mm diameter spheres, the surface roughnesses of the test specimens increases drastically from L/D values equal to 4, while that, for boring bar filled with 10.32 mm spheres, the roughness varies little. Figure 4 (b) presents the average RMS acceleration values of the tool during the turning operations. It is noticed that, as expected, they behave similarly to the surface roughness.

The tool holders filed with 9 and 10 mm spheres got into an unstable mode for L/Ds equal to or greater than 4, where it can be noted that the acceleration signal, that is, the tool vibration, grows exponentially as the tool overhang increases. When the boring bar filled with 10.32 mm spheres, both the surface roughness and the acceleration presented reasonable values until an L/D equal to 6. This result indicates that the mass of the particles in the cavity may have a greater effect on the damping than the value of the clearance between the particles and the cavity wall, once that, as the particle diameter increased, and thus its mass, the spacing between the particles and the cavity's wall decreased.

Then, the boring bar with a cavity filled with 10.32 mm diameter spheres, which had the best performance among the boring bar filled with spheres, had its performance compared to the ones of the conventional boring bar and of the boring bar with an empty cavity. Figure 5 (b) enables comparing the tool accelerations when each configuration of the boring bar is employed. It is seen that the acceleration of the boring bar filled with Ø 10.32 mm diameter spheres remained practically constant for all tested overhangs and, correspondingly, both the surface roughness and the geometric profile of the machined surface did not deteriorate within the test limits, as shown in figure 5 (a). As for the conventional boring bar, it vibrated significantly at L/D equal to and greater than 3.4. Therefore, it is possible to use a boring

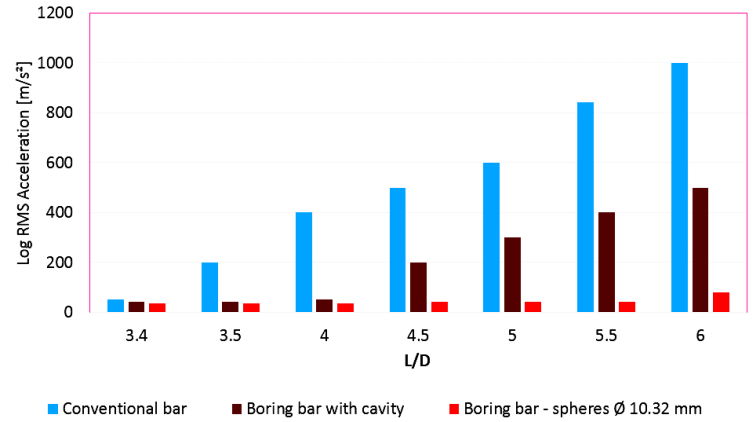

(a)

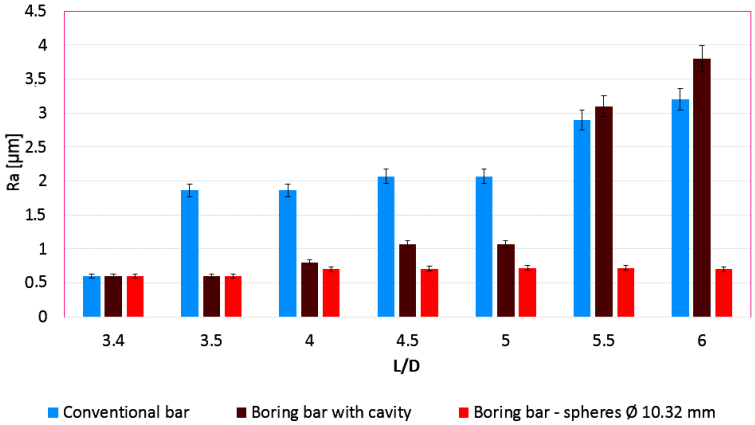

(b)

Figure 5. (a) Acceleration values and (b) average surface roughness (Ra) obtained with the conventional bar, the boring bar with a cavity and the boring bar filled with Ø 10.32 mm steel spheres.

bar with a sphere filled cavity at L/D values up to 6, whereas for the conventional boring bar it is not advisable to exceed the L/D value of 3.4. This indicates that it is possible to perform internal turning operations using 20 mm diameter boring bar filled with spheres with overhangs up to 120 mm – and not 68 mm, which is the stablished conventional limit for this system.

The tests showed essentially that, as may be seen in figures 5 (a) and (b), the steel boring bar can exceed a L/D equal to 4 recommended by some tool makers [8, 21-23] with a gain above 50 % when a particle impact damper is used. This greater overhang equals the overhang limit for cemented carbide boring bars, which is around a L/D value of 6 – That allows of replacing cemented carbide boring bar with steel boring bar filled with spheres. By making a cavity inside the steel tool holder, that substitution is rendered possible, reducing costs and increasing efficiency. It is convenient to note that it was not possible to verify whether a boring bar with a PID may attain the performance of an anti-vibration one, which allows for a L/D equal to 10 [8]. The length of the boring bar employed did not render that test possible, because of the constraint that, to guarantee a rigid fixation, the length of the boring bar fixed inside the machine turret should be at least four-times its diameter.

The main points to be highlighted based on the results shown are:

- Tool vibration remained almost constant with the increase of the tool overhang up to the point it suddenly increased in a certain value of tool overhang (called limit value for stable cutting). Small changes in the tool overhang close to the

limit region generated this sudden variation, indicating that the tool bar is very sensitive to the rigidity change in this range of overhang;

- the use of internal turning tool bars with impact damper caused an increase of the limit value for stable cutting and, consequently, made possible the turning of deep holes;
- As the diameter of the spheres increased, the limit value for stable cutting also increased, indicating that the damping effect is higher when the mass of the spheres is higher and the gap between the spheres and the cavity wall is lower, which cause, the increase of the impact momentum transfer.
- when the sphere diameter used in the impact damper was 10.32 mm it was not possible to determine the limit value for stable cutting in terms of tool vibration, because it was possible to cut up to a L/D value of 6 without sudden increase in the acceleration signal. We could not go higher with the L/D value in these experiments, since, above this tool overhang, it was not possible anymore to hold the bar in the lathe turret in a safe way.

Based on these results it can be stated that the vibration energy dissipation (damping effect) caused by the impact of the spheres against the cavity wall is higher when the spheres have higher mass associated to the decrease of the gap between spheres and the cavity wall. The impact of these spheres against the wall transfers a high amount of linear momentum from the tool bar containing the cavity to the spheres. The damping effect depends on the variation of the linear momentum during the impact of the sphere, which, in turn, depends on the sphere material, mass, the speed of the sphere at the impact moments and the restitution coefficient of the impact. Since this last parameter was the same for all bar configurations (the materials of the spheres and of the tool bar were the same for all types of bars), the linear momentum depends on the spheres mass (which increased a lot with a little increase of the sphere diameter), the sphere speed at the moment of contact between the sphere and the wall and the number of collisions between these elements (collisions with wall speed in opposite sense to the sphere speed). What the results of the experiments showed is that the increase of sphere mass (or sphere diameter) and the decrease of the gap (which may have increased the number and frequency of impacts between the elements) caused a higher damping effect of the sphere impacts against the cavity wall. Therefore, the impact damper, which used the biggest spheres, was the one, which caused the highest damping effect and, consequently was able to cut with the longest tool overhang.

Another important point to evaluate the damping capacity of the impact damper is the mass ratio between the spheres inside the cavity and the mass of the vibrating body (the tool bar). As the sphere masses increased, this ratio also increased and, consequently, increased the amount of material to cause the damping effect of the toolbar.

It can be observed in figure 6 that the peak excitation frequencies of the tool during the machining process, obtained by applying the Fast

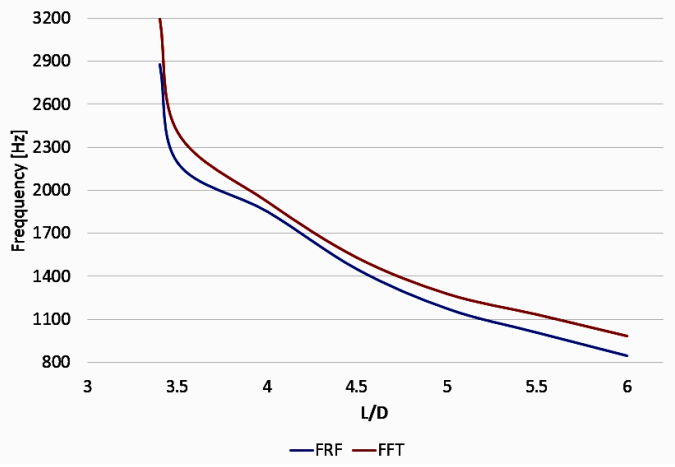

Figure 6. Comparison between the FRF and the FFT of the boring bar with the best performance (boring bar filled with Ø 10.32 mm spheres).

Fourier Transform (FFT) to the tool vibration signals obtained during the machining operation with the boring bar filled with 10.32 mm spheres, are very much similar to the natural frequency of the tool (FRF) obtained from the impact tests. Both decrease as the tool overhang increases. Therefore, as the tool overhang increases, the deflexion caused by the cutting forces also increases and, consequently, both the excitation and natural frequencies decrease. However, as it may be seen in figures 4 and 5 (b), that vibration increases little, probably due to the damping caused by the spheres impacting against the cavity's walls. Consequently, the surface roughness obtained when using this boring bar also remains in an adequate level.

5. CONCLUSIONS

Based on the results that were exposed and discussed in this work, it may be concluded that, in the internal turning of hardened steel with conventional boring bar and boring bar with impact dampers:

- The damping capacity of the damper used in this work is such that it allows of using boring bar L/Ds way greater than the ones recommended for conventional boring bar, thus making the internal turning of deeper holes possible;
- The L/D of the boring bar can be increased when using spheres whose diameter is a little less than the diameter of the cavity in the damped tool holder, when compared to the boring bar filled with smaller spheres;
- The impact damper is able to compensate the mass loss of the boring bar with a cavity and, consequently, its loss of stiffness and change in natural frequency. That makes obtaining good surface finishes of the machined parts possible, while using grater L/Ds than the ones recommended for conventional boring bar.

ACKNOWLEDGMENTS

This research was supported by the European Union and the Hungarian State, co-financed by the European Regional Development Fund in the framework of the GINOP-2.3.4-15-2016-00004 project, aimed to promote the cooperation between the higher education and the industry.

REFERENCES

[1] X. Ajay Vasanth, P. Sam Paul, G. Lawrance & A.S. Varadarajan, Vibration control techniques during turning process: a review. *Aust J Mech Eng* 00, 1–21 (2019).

[2] Albuquerque, Marcos V., "Modelagem e Análise Dinâmica de um Absorvedor de Vibrações por Efeito de Impacto", Dissertação de Mestrado, Universidade de Campinas, Campinas, 2016

[3] UNGAR, E, "Damping of Panels", Noise and Vibration Control, Chap 14. In: Beranek, L., McGraw-Hill, Washington, USA, 1988.

[4] Bustamante, Marcelo A. S., "CARACTERÍSTICAS DISSIPATIVAS DE AMORTECEDORES DE PARTÍCULAS DE ELASTÔMERO" Tese de Doutorado, UFSC, Florianópolis Santa Catarina, Brasil, 2014.

[5] Suyama, Daniel I. "Uma contribuição ao estudo do torneamento interno em aços endurecidos", Tese de Doutorado, UNICAMP, Campinas, São Paulo, Brasil, 2014

[6] Bavastri, C. A., 1997, "Redução de Vibrações de Banda Larga em Estruturas Complexas por Neutralizadores Viscoelásticos", Tese de Doutorado, UFSC, Florianópolis Santa Catarina, Brasil,1997

[7] Rubio, L.; Loya, J.A.; Miguélez, M.H. e Sáez, J.Fernández. "Optimization of passive vibration absorbers to reduce chatter in boring" Mechanical Systems and Signal Processing, p. 691 - 704, Madri, Espanha, Agosto, 2013.

[8] SANDVIK. "Silent tool for turning: overcome vibrations in internal turning", Disponível em: < http://www.sandvik.coromant.com/en-us/products/silent_tools_turning>. Acesso em: 15 de maio. 2017.

[9] Olson, Steven E.,Drake, Michael L, "Development of Analytical Methods for Particle Damping" University of Dayton Research Institute, Ohio, USA,1999

[10] DUNCAN, M. R., WASSGREN, C. R. & KROUSGRILL, C., "The damping performance of a single particle impact damper". Journal of Sound and Vibration, v.286, p. 123–144, 2005, West Lafayette, USA

[11] Sanap, SB, Bhave, SY, Awasare, PJ, "Impact damper for axial vibration of a continuous system", Proc IMechE Part C: J Mechanical Engineering Science, Vol. 230(13) 2145–2157 Londres, Inglaterra, 2016

[12] Booty, C, Bowyer, E.P. Krylov, V.V. "Experimental investigation of damping flexural vibrations using granular materials" International Congress on Sound and Vibration Department of Aeronautical and Automotive Engineering, Loughborough University, Loughborough, Leicestershire, Inglaterra, 2014.-

[13] Papalou A, Masri S F, "Response of impact dampers with granular materials under random excitation", Earthquake Engineering & Structural Dynamics, Technological Educational Institute of Western Greece, Greece, Greece, 1996

[14] Panossian H V, “Non-obstructive particle damping: new experiences and capabilities”, Proceedings of the 49th AIAA/ASME/ASCE/AHS/ASC, Structures, Structural Dynamics and Materials Conference, Califórnia, EUA 2008.
[15] Panossian H V, “Structural damping enhancement via non-obstructive particle damping technique”, ASME Journal of Vibration and Acoustics vol. 114, (1992), pp. 101–105, Califórnia, EUA
[16] Zheng Lu, Sami F. Masri, Xilin Lu, “Parametric studies of the performance of particle dampers under harmonic excitation”,State Key Laboratory of Disaster Reduction, Civil Engineering, Tongji University, Shanghai, China, 2009
[17] Friend, R. D., Kinra, V. K, “Particle Impact Damping”, Journal of Sound and Vibration, xxxxx 233(1), pp 93-118, 2000.
[18] Xu, Z., Wang, M. Y., “PARTICLE DAMPING FOR PASSIVE VIBRATION SUPPRESSION: NUMERICAL MODELING WITH EXPERIMENTAL VERIFICATION”, Design Engineering Technical Conferences and Proceedings of DETC’03 ASME 2003, Illinois, Chicago, USA, 2003
[19] Okubo, N. Yoshida, Y., Hoshi. T.,“Application of Modal Analysis to Machine Tool Structures”, CIRP Annals - Manufacturing Technology
[20] SANDVIK. Modern Metal Cutting: A Pratical Handbook. Suecia: Sandvik Coromant Technical Editorial, 2010.
[21] KENNAMETAL, “Catálogo Metalworking Solution& Services Group”, 2010 Disponível em <http://www.maximtools.ro/images/produse/kennametal/prelucraregauri/cataloage/A-09-02148EN_tunable_boring_ bars.pdf>. Acessado em: Acessado em:12/02/2017.
[22] KENNAMETAL, Catálogo, , “WIDIA tooling Systems”, 2012 Disponível em: <https://www.widia.com/content/dam/kennametal/widia/common/resources/downloads/literature/WIDIA%20Catalogs/WIDIA%20Tooling%20Systems%202012%20Catalog/A-09-02122_Widia_ToolingSystems_complete_EN.pdf>. Acessado em:12/02/2017.
[23] SANDVIK,“Modern Metal Cutting: a Practical Handbook”, Sandviken, Suécia, 2016

NANOMATERIALS SCIENCE & ENGINEERING
Vol. 2, No. 3, pp. 135-143 (2020)

RESEARCH ARTICLE

https://doi.org/10.34624/nmse.v2i3.19554

Improvement of active layers homogeneity for the MEA's (Membrane Electrode Assembly) of PEMFC (Proton Exchange Membrane Fuel Cell): impact of the ink quality formulation

TEAV Carine[1,2], NAYOZE-COYNEL Christine[2,*]

[1] Grenoble INP – Pagora, 461 Rue de la Papeterie, 38402 Saint-Martin-d'Hères, FRANCE
[2] French Alternative Energies and Atomic Energy Commission (CEA) – 17 Avenue des Martyrs 38000 Grenoble, FRANCE
**Corresponding author, e-mail address: christine.nayoze@cea.fr*

Received 22 July 2020; accepted 16 September 2020; published online 22 September 2020

ABSTRACT

This study focuses on the improvement of active layers for PEMFC (Proton Exchange Membrane Fuel Cell) fuel cells. These active layers (anode and cathode) constitute the core of the cell where chemical reactions take place. The goal is to improve the performance and durability of these cells by working on these layers. Some research has shown the impact of homogeneity of active layer on fuel cell performance by working on printing processes. In our case, the aim was to obtain homogeneous active layer after coating deposition process by studying the formulation of the ink: the order of introduction of components and the dispersion processes. Several ink dispersion processes stood out, including a planetary mixer that gave satisfactory results in terms of particle size and deposit homogeneity. Moreover, the order of introduction of the components during the ink formulation seem to have an impact onto rheological parameter and also onto particles size.

1. INTRODUCTION

Nowadays, environmental issues are becoming more and more important in our society. Ecology and global warming are at the heart of these issues and play an important role in the automotive market. Today's society is seeking to reduce oil consumption in all areas but specifically in the automotive industry. Proton Exchange Membrane Fuel Cell (PEMFC) is an electrochemical cell allowing to environmentally friendly convert energy to replace the use of fossil fuels. This cell produces electricity through the oxidation of hydrogen (H_2) at the anode and the reduction of oxygen (O_2) at the cathode. The heart of the fuel cell, Membrane Electrode Assembly (MEA), is composed of an exchange membrane which is surrounded by two catalyst layers, an anode and a cathode. This part of the fuel is very important and has a real impact on cell performance and lifetime. Catalyst layers are composed of a catalytic powder of platinum-based nanoparticle deposited onto carbon support, ionomers, water and solvents. Several methods exist to print these layers: bar-coating, screen-printing, electrospray coating among others and Roll-to-Roll coating for a large scale. After being obtained, these actives layers are hot-pressed onto a membrane and assembled with Gas Diffusion Layer (GDL) in order to get the MEA. As the MEA gets thinner and thinner (membrane of 10 µm or less, decreasing of the active layer thickness due to the reduction of the catalyst loading) and with the

objective not to have an impact onto the performance and durability, active layer must be as homogeneous as possible, without defects as agglomerates or cracks. Indeed, agglomerates in these layers could lead to damages on durability with deformation and rupture of the membrane. The formation of agglomerates could be favoured by different factors: the solvent used in the formulation as showed in the study of *D. Huang et Al*. [3] who have worked on the effect of solvent in catalyst ink on PEMFC performance, the catalytic powder which could also favour agglomerates [4] and contribute to heterogeneous active layers. The ideal is to find the right formulation so that the ionomer used is also well dissolved in the solution and the catalyst powder well dispersed. Indeed, the latter would have a different degree of polymerization and would result in a different structure that could lead to agglomeration as *T. Kim et Al.* [5] have highlighted in their work. The way of disperse could also facilitate the formation of agglomerates: *M. Wang et Al*. [6] have studied different time of dispersing the catalyst ink: it was dispersed with the ultrasonic bath at different time and speed. They have shown the importance to well dispersed ink and have been able to correlate catalyst agglomeration and fuel cell performance. C. Jeffery Jacobs [7] has also studied the influence of catalyst ink mixing procedures on PEMFC performance and especially has worked on three methods of dispersion: bead milling, high shear stirring and ultrasonic bath. He has observed an effect of the dispersion method on catalyst layer formulation, structures and agglomerates observed in the active layers. Only few studies have been carried out on ink process dispersion and the order of introduction of ink. That is why, research on how to avoid agglomerates into inks by working on formulation procedures could be interesting. This study will focus on the order of introduction of components for formulating the ink and three processes of ink dispersion: a high shearing mixing, a mechanical dispersion and planetary mixers. The aim is to optimize the ink formulation and to have homogeneous active layers. Moreover, one of our goal is both to obtain a viscosity above a certain threshold (at least 10 Pa.s), in order to be adapted to printing processes as screen-printing and bar coating, but at the same time to have a particle size below 1 µm.

Our results will show differences, in particular in the structure of the active layer but also in rheological aspects through characterisations.

2. EXPERIMENTAL PROCEDURE

The cathode-type catalytic ink was manufactured according to the following protocol. The first phase consists in dispersing TEC10V50E catalytic powder of platinum deposited onto carbon support Vulcan XC72 (Pt/C) (47.2wt%Pt, Tanaka®) in distilled water. The handling is carried out in a “glove box” due to nanoparticle risks in the catalytic powder. Once the powder has been dispersed in water; two PFSA polymers (ionomer 1 Nafion® *D2020*, ionomer 2), as well as the solvent (ethanol), can be added under suction. The ratio between ionomer and carbon is I/C=0,8.

Once the ink has been dispersed, it is placed under magnetic agitation at least one day before being used and characterised. The method used in this study to obtain the deposit is bar coating with a liquid thickness of 40 µm and a drying temperature at 40°C. The catalytic inks contain dry content of 23% linked to the use of bar-coated or

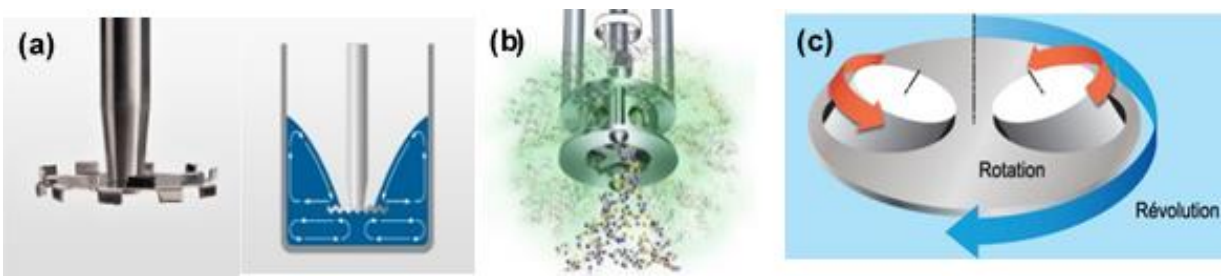

Figure 1. Operating principles of the different processes – (a) Disc Dispersal, (b) Module Rotor/Stator for high shearing mixing, (c) Planetary mixer system (Rot/Rev).

screen-printing processes. The catalyst loading in the active layer is 0,25 mgPt/cm².

2.1. PROCESS OF DISPERSION

Three dispersion methods have been tried, including mechanical dispersion (Dispermat®), high shear dispersions (Silverson®) and planetary mixers (Mazerustar from Kurabo® and Kakuhunter from Sodipro®) without mechanical modules into the flask of ink for the latter. At total, 4 different tools have been tried.

Mechanical dispersion from Dispermat® (*Disc Disp.)* is the process used as reference in the laboratory. It is a mechanical dispersion generated by a dispersal disc as shown in the figure 1.(a). The tests were carried out at 4000 rpm during 15 min. Silverson® (*Rotor/Stator*) constitutes a high shearing mixing. The modulus dispersion works on a rotor/stator system (moving part inside) with some open area on the side that can have different shapes (square, rectangular…) and does not move. The liquid goes inside the module from below and a high shear rate is created when the liquid come out the holes. The ink was mixed at 6000 rpm during 10 min (figure 1.(b)).

Planetary mixers work on the rotation of the container on itself in one direction and the revolution of the container around an axis in the opposite direction (figure 1.(c)). These two parameters are independent but a ratio (rotation on revolution) could be controlled. There is no dispersal disc inside containers. The biggest difference between the two planetary mixers is the wide range of levels of rotation/revolution for the Mazerustar (from 0,1 to 0,9) taken at 0,9 for the study (Rot/Rev 0,9) and the fixed ratio of 0,4 for the Kakuhunter (Rot/Rev 0,4).

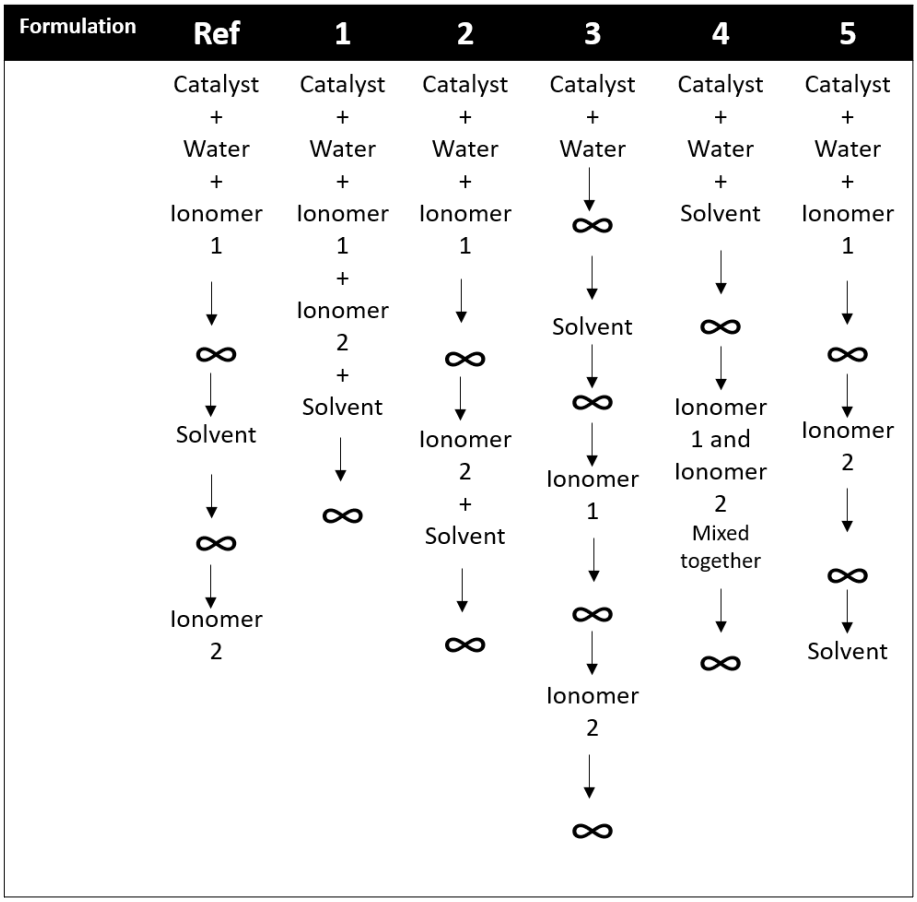

Figure 2. Five formulations carried out to study the order of introduction of components in ink formulation compared to the formulation of reference (Ref).

After being mixed by one of these dispersion processes, at least one day under magnetic agitation is necessary for the mixture stabilization.

2.2. ORDER OF INTRODUCTION

The influence of the order of introduction of the components in the ink was tested to see if any sequence favoured the appearance of agglomerates. The figure 2 shows the different formulations carried out, named from 1 to 5 compared to the formulation of reference (Ref) used before the study in the laboratory. The symbol ∞ corresponds to the moment of the mixing.

The formulation of reference (Ref) corresponds to a first mixing of powder, water and ionomer 1; in a second part, solvent is introduced and another mixing is carried out, ionomer 2 is added at the end. The formulation 1 corresponds to an introduction of all components into the container before dispersion. In formulation 2, ionomer 2 and the solvent are added together before dispersion. The formulation 3 corresponds to a dispersion between each addition of component. The formulation 4 proposes a pre-mixing between the ionomers before added to the mixture of catalytic powder and water. The formulation 5 reverses the order of introduction between ionomer 2 and solvent compared to the formulation of reference.

2.3. CHARACTERISATION

Several characterisations are carried out on the ink. First, a Kinexus rheometer was used to measure the following parameters: viscosity, flow threshold, viscous and elastic moduli. Rheological parameters measurements are essential to make the link between the formulation and the nature of the ink and whether or not it promotes the presence of agglomerates. For example, an ink that is fairly liquid less than 1 Pa.s will tend to sediment and therefore lead to ink heterogeneity. A more viscous ink will tend to be more stable over time.

The viscosity was determined for a shear rate sweep between 1000 s^{-1} and 0,01 s^{-1} and the viscosity value for comparison is noticed at a shear rate of 0,5 s^{-1}. The measure of amplitude oscillation enables to know the behaviour of the sample by measuring elastic (G') and viscous (G'') components. On the graphic, you have to look at the left side of the curves before the deformation becomes too large and destroys the ink. The closer the phase angle between the viscous and elastic moduli is near to 0°, the more the ink will behave like a solid and be stable. The amplitude oscillation measurement was performed for a strain between 0,1 Pa and 100 Pa. The frequency oscillation allows the stability of the ink to be investigated. The lower and the more constant the value of the

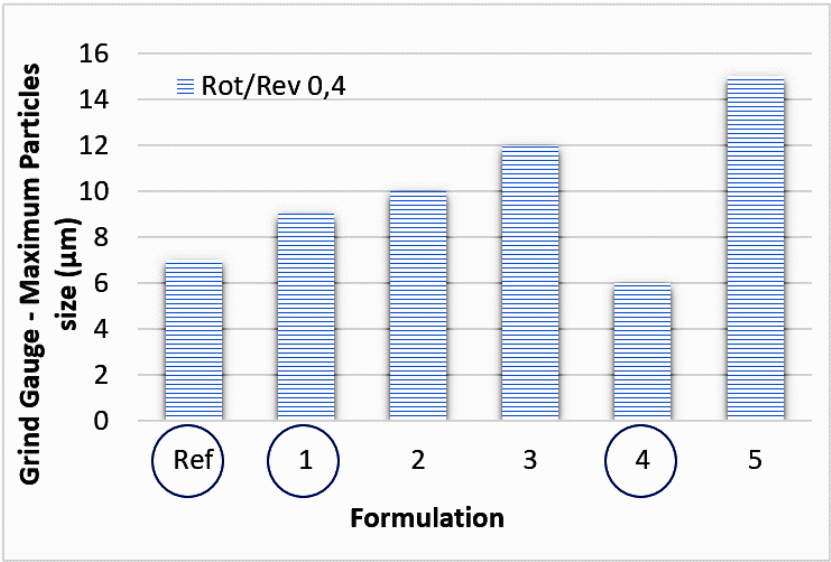

Figure 3. Graphic of the maximum particle size with grind gauge (µm) in function of the six formulations using planetary mixer Rot/Rev 0,4.

"phase angle" between the viscous and elastic components is, the more stable the sample will be and will behave as a solid. The frequency oscillation measurement was performed for frequencies between 0,1 Hz and 100 Hz at different strain values according to the value taken in the constant zone of the amplitude oscillation curves.

A grind gauge gives an idea of the maximum particle size in an ink and enable to eliminate inks with very large sizes. An electro-acoustic probe (EAP) was used to obtain an average particle size distribution in the ink. This ultrasonic scattering method consists in determining the particle size distribution of a non-diluted dispersion by measuring the attenuation of ultrasound at frequencies between 1 MHz and 100 MHz.

After being coated on a PTFE Teflon® substrate using the bar coating, the deposit was observed thanks to a scanning electron microscope (SEM). Agglomerates and homogeneity could be studied.

3. RESULTS & DISCUSSION

3.1. INK CHARACTERISATION

3.1.1. Selection of inks

The order of introduction of components has been modified for each formulation. Characterization was carried out using a grind gauge to eliminate the inks with the largest particle sizes. Figure 3 shows the maximum particles size for the 6 formulations dispersed with the planetary mixer - 0,4 (Rot/Rev 0,4). Formulations 2, 3 and 5 were exited from the rest of the study because of the highest particle sizes and the closed ways of formulation.
Formulations Ref, 1 and 4 were selected based on the results obtained with the grind gauge (minimum particles size) and some more complete characterizations have been done with these formulations.

3.1.2. Particles size and viscosity results

Inks were characterized through EAP to determine the mean particles size and the rheometer to measure the viscosity. Figure 4.(a) shows mean size particles in microns in function of the formulations Ref, 1 and 4 for the four dispersion processes. Figure 4.(b) shows the ink viscosity in function of the formulation Ref, 1 and 4. The reference (Disc Disp.) process is also integrated in these graphs to compare to the other processes with it.

First trend, smaller particle sizes were observed for the other dispersion processes (less than 10µm) compared to the reference process (Disc Disp.) for the formulation of reference (Ref) (around 16 µm), showing an improvement due to the dispersion process. Moreover, the way of dispersing seems to play on the size of the particles. Planetary mixer – 0,9 (Rot/Rev 0,9) allows a more homogeneous dispersion with particle sizes below 1 µm whatever the formulation (figure 4.(a)). Concerning the other dispersion processes, there is a correlation to be made between the formulation and the process because different particle sizes are obtained.

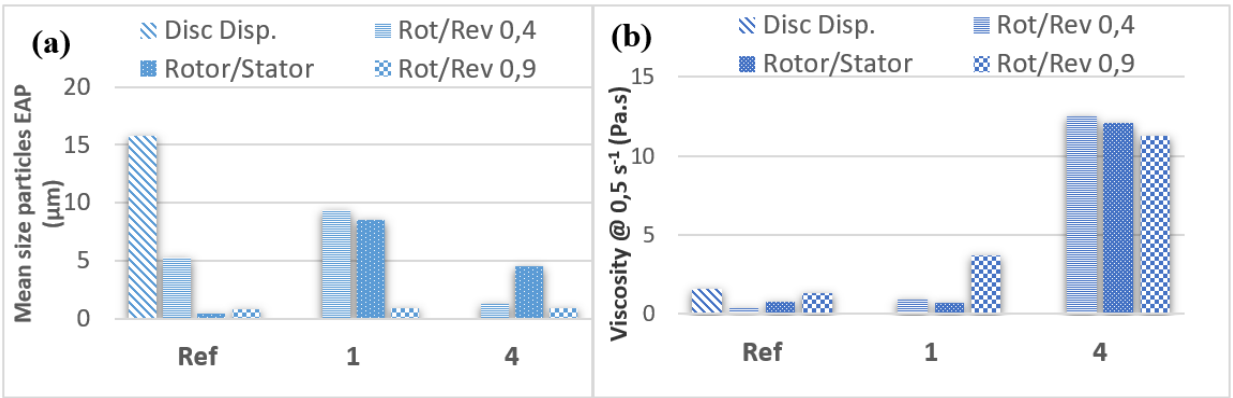

Figure 4. (a) Particle size (µm), (b) Viscosity @ 0,5 s^{-1}(Pa.s), measured for the formulations Ref, 1 and 4 and for the four dispersion processes.

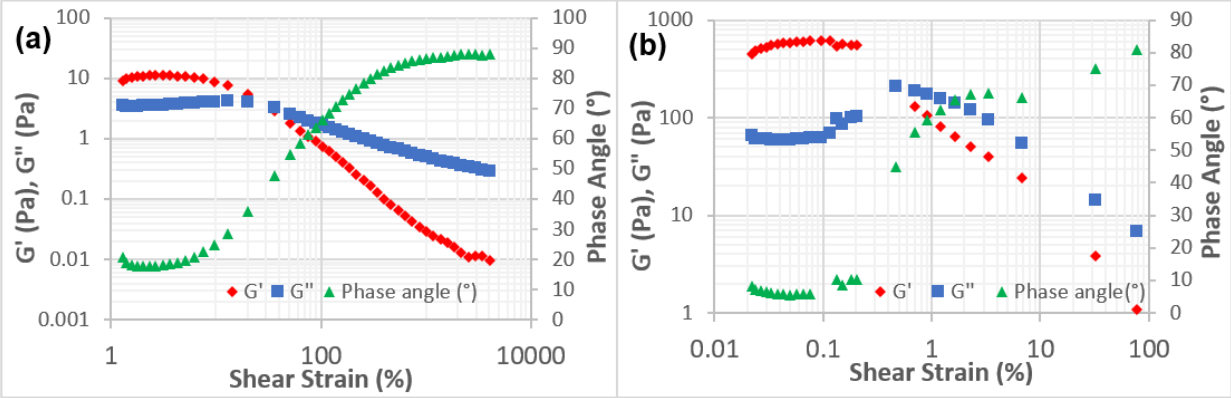

Figure 5. (a) Amplitude oscillation for formulation 1 ((low viscosity: 0,9 Pa.s), (b) Amplitude oscillation for formulation 4 (high viscosity: 12,5 Pa.s), both mixed with the planetary mixer – 0,4 (Rot/Rev 0,4).

Formulation 1 seems not to be adapted for the planetary mixer – 0,4 and rotor/stator processes with mean particles size around 9 µm. This latter was found to have good particle size for formulation Ref (around 900 nm). However, the rotor/stator process will not be held for a number of other reasons. In fact, it seems that it is a suitable method for a very liquid ink with a viscosity of less than 1 Pa.s. The shear performed will allow a better dispersion for a non-viscous ink. However, for our application, we need an ink with a viscosity between at least 10 to 50 Pa.s, adapted to our printing process. On the other hand, the planetary mixer Rot/Rev 0,4 did not have excellent result for the formulation Ref.

Other trends are noticed. Formulation 4 allows to obtain a more viscous ink (between 11 and 13 Pa.s) than the other formulations whatever the processes used (figure 4.(b)). Moreover, it can be seen that the particle sizes are smaller for this formulation 4 in general. One hypothesis would be that pre-mixing the two ionomers increases the viscosity of the ink and the mixing of powder, water and solvent allows a better dispersion of particles at the first step. The ionomers would bind more between the particles, allowing a better interaction and increasing the viscosity of the formulation. This is quite interesting: in fact, according to the printing process, it could be possible to have a more or less viscous ink according to the order of introduction of components.

Viscosity and particle size seem so to be related. The trend is that the particles size will be as smaller as the viscosity will be high. Indeed, more liquid inks (having a viscosity lower than 1 Pa.s) will tend to destabilize more quickly and therefore, the particles are likely to sediment or agglomerate. That is why, it is always recommended to leave under magnetic agitation to avoid sedimentation.

3.1.3. Rheological results

The figure 5 shows amplitude oscillations measured with the rheometer for the planetary mixer Rot/Rev 0,4. It compares the trends between two formulations having significantly different viscosity: formulations 1 with a low viscosity of 0,9 Pa.s and formulation 4 with a higher viscosity of 12,5 Pa.s in the aim to establish a link between viscosity and stability of the ink.

The curves obtained for the oscillation amplitude allow to highlight the viscoelastic behaviour of our inks. However, the fact that the elastic component G' is higher than the viscous component G" shows that the elasticity is preponderant compared to the viscous aspect. The ink is then viscoelastic – solid for the formulation 1 and 4. Nevertheless, we can notice that values of G' are quite different between the two formulations. Formulation 1 has a modulus G' of around 10 Pa, contrary to formulation 4 which has a modulus at around 600 Pa. The higher the value of the elastic component G', the more stable the formulation will be. Indeed, the elasticity maintains the structure of the samples. Moreover, if we compare the phase angles of the amplitude oscillation graphs, we obtain a phase angle of about 18° for formulation 1

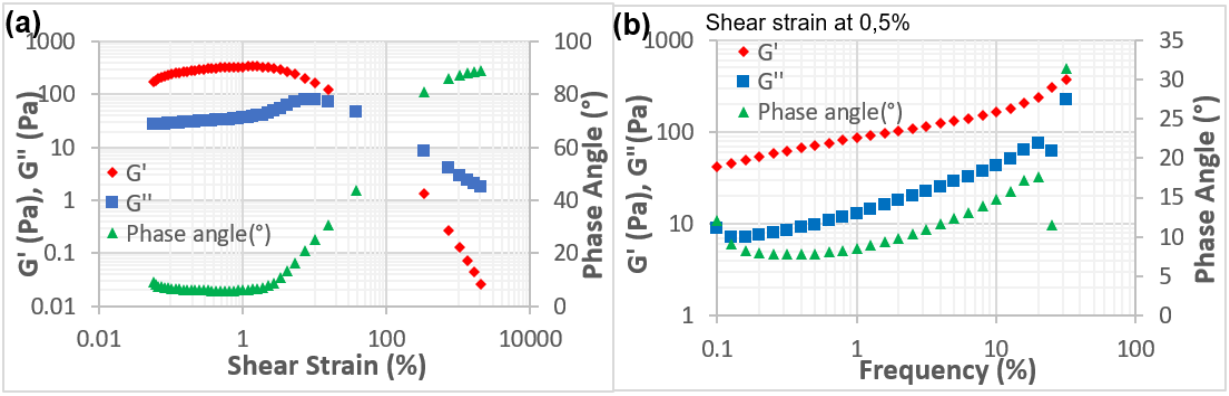

Figure 1: (a) Amplitude oscillation (b) Frequency oscillation for formulation 1 with the planetary mixer – 0,9 (Rot/Rev 0,9)

(figure 5.(a)), compared to a phase angle around 5° for formulation 4 (figure 5.(b)). The closer this curve is to 0°, the more the sample will behave like a solid. We have the solid behaviour/stability and viscosity relationship. Frequency oscillation has also been measured and confirm the non-stability of the less viscous ink.

The two remaining processes are the two planetary mixers with the different ratios. The planetary mixer with a high ratio of 0,9 (Rot/Rev 0,9) presents highly satisfying results whatever the formulation with particle sizes below 1 µm each time (figure 4.(a)). A higher ratio allows a more homogeneous and stable mixture to be obtained over time.

The rheological curves show a more obvious stability for the planetary mixer with a high ratio of 0,9 (figure 6). It shows an angle phase close to 5° on the constant zone in the amplitude oscillation graph. Moreover, the plate is longer as the deformation progresses, characterizing a more stable behavior than the rot/rev 0,4 on figure 5.(a). The frequency oscillation on the right also confirms this statement with a phase angle quite constant at the beginning. These results have also been shown for the formulation of reference (Ref) with a longer plate zone on oscillation amplitude characterizing stability.

In this study, considering the nature of the components used and the ratio between the components, the planetary mixer, more precisely with the ratio Rot/Rev 0,9, seems to be the best method of dispersing inks for catalytic layers for application of screen printing and bar coating processes. It was seen in figure 4.(a) that the particle sizes were particularly small (less than 900 nm) for the three formulations which also have different rheological properties. However, we noticed many differences in structure, especially when the deposition is observed at SEM.

3.2. SEM RESULTS

After being coated on substrate, surfaces of the active layers have been observed with SEM.

3.2.1. Process dispersion comparison

Active layers surfaces made with the reference formulation (Ref) with the four methods of dispersion were observed (figure 7) using a SEM. The mechanical dispersion seems to produce many agglomerates, as well as the planetary mixer with a ratio of 0,4 which present maximum particles size of 80 µm. The high shear rate dispersion (Rotor/Stator) presents a lot of cracks, which makes the layer non-homogeneous. The cracks length can reach 100 µm or more. However, cracks may allow gases to pass through more quickly and also allow water to be evacuated easier. But these cracks are places where chemical reactions cannot take place and, therefore, could produce less energy and be less performant. Moreover, these cracks can create significant deformations in the membrane during the transfer of the active layers

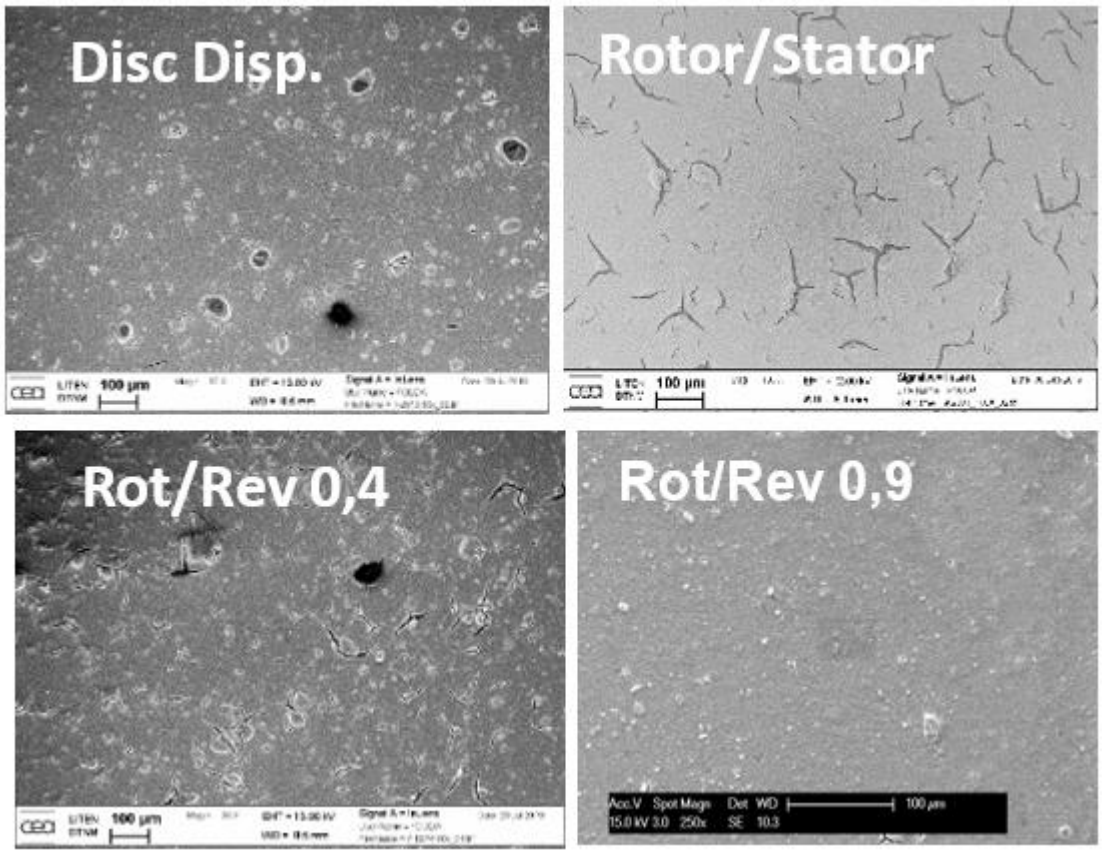

Figure 7. SEM images comparing the different processes for the reference formulation (Ref) (magnification: x250).

to the membrane and create weaknesses and holes. The deposit from which the ink has been dispersed with the planetary mixer – 0,9 presents few agglomerates and the maximum agglomerates size is 20 µm. It is mostly more homogenous. A higher ratio allows to have a better mixing of the ink and to not create agglomerates.

These images appear to correlate well with trends obtained from the EAP. However, the size of particles measured at the SEM do not match. The size of the agglomerates observed on SEM are higher than the one measured with the EAP. Other factors may come into play, such as drying conditions, which may also promote cracks and agglomerates.

The results appear to be good for the planetary mixer – 0,9. The results in section 3.1 showed that the particle sizes were relatively small regardless of formulations Ref, 1 and 4. However, rheology's parameters are different.

3.2.2. Formulation comparison using planetary mixer Rot/Rev 0,9

The figure 8 shows the active layer surface observed at SEM for the formulations 1 and 4 compared to the reference formulation (Ref) for a same dispersion process, the planetary mixer Rot/Rev 0,9. The aim is to show the impact of the order of component introduction into the ink for a same dispersion process. The pictures show that formulation 1 presents many heterogeneities (maximum size of agglomerate: 40 µm). Formulation Ref and 4 have also agglomerates but the surface is mostly more homogeneous with a maximum agglomerates size of 20 µm. In a general way for the observed samples, the maximum size measured on the SEM surfaces doesn't correlate, in term of value, with the maximum size particle measured with the EAP. This can be explained by the fact that the parameters of the coating process cannot be optimized and can lead to particles

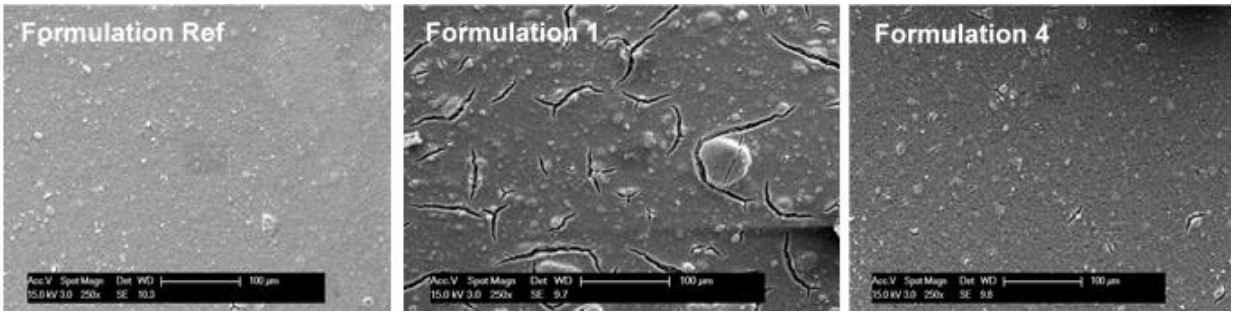

Figure 8. SEM images comparing formulations Ref, 1 and 4 for the planetary mixer 0,9 (magnification:x250).

agglomeration. The deposition method, the drying temperature and speed as well as the evaporation temperature of the solvent can influence on faults. If this latter is too high or too low, cracking or clumping may occur.

However, formulation of reference and formulation 4 could may both be suitable to the planetary mixer 0,9 to have a homogenous active layer. But if we look at rheology and especially the viscosity of inks, our application in screen printing or bar coating would more suit with a high viscosity. The formulation 4 will so be more adapted.

4. CONCLUSION & PERSPECTIVES

This study has dealt with the way of formulating the active layer's ink: the order of introduction of components but also the way to disperse. It was carried out on an ink including two ionomers. Better results were obtained for processes other than the reference process (Disc Disp.) for the reference formulation (Ref). Three other processes of dispersion were tested. They differ by their methods (high shear rate, planetary mixers….) but also by their mixing speed (ex: planetary mixers with ratio rotation/revolution 0,4 and 0,9). A higher ratio and speed have demonstrated that the ink could have a better homogeneity both in ink and on deposit. The planetary mixer with a ratio Rot/Rev 0,9 process was chosen as the most appropriate in our situation.

In addition, the particle size can be reduced thanks to the order in which the components are introduced. It has shown that formulation can play on rheological parameters, as the viscosity or the stability of the ink by interpreting the amplitude and frequency oscillations. The particle size seems to be linked to the viscosity: higher is the viscosity, smaller will be the particles. Moreover, the formulation 4, allowing a high viscosity due to a dispersion of the catalyst in the water and solvent and a pre-mixing between the ionomers, was also found to be suitable for our coating method.

To go further in this study, cross sections of catalytic layers are going to be made to observe and characterize the structure of the active layer. Single cell performance tests will also be carried out in order to see the impact of all these parameters and in particular the agglomerates.

REFERENCES

[1] Hui Xu, Chao Lei, Zachary Green, Tom McCallum, *Ionomer Dispersion Impact on Fuel Cell and Electrolyzer Performance and Durability (SBIR Phase II TTO)*, Department of Energy, Auburndale USA (2018).

[2] Eunae Lee, Do-Hyung Kim, Chanho Pak, *Effects of cathode catalyst layer fabrication parameters on the performance of high-temperature polymer electrolyte membrane fuel cells,* Graduate Program of Energy Technology, School of Integrated Technology, Institute of Integrated Technology, Gwangju Institute of Science and Technology, Gwangju 61005, Republic of Korea (2020).

[3] De-Chin Huang, Pei-Jung Yu, Feng-Jiin Liu, Shu-Ling Huang, Kan-Lin Hsueh, Yen-Cho Chen, Chun-Hsing Wu, Wen-Chen Chang, Fang-Hei Tsau, Effect of Dispersion Solvent in Catalyst Ink on Proton Exchange Membrane Fuel Cell Performance (2011).

[4] Mathieu Lepesant. Catalyseurs multimétalliques nano-organisés pour pile à combustible PEM. Matériaux. Université de Grenoble, 2014. Français. ffNNT : 2014GRENI052ff. fftel-01131225f

[5] Tae-Hyun Kim, Jae-You Yi, Chi-Young Jung, Euigyung Jeong, Sung-Chul Yi, *Solvent effect on the Nafion agglomerate morphology in the catalyst layer of the proton exchange membrane fuel cells*, (2016).

[6] Min Wang, Jae Hyung Park, Sadia Kabi, K.C. Neyerlin, Nancy N. Kariuki, Haifeng Lv, Vojislav R.

Stamenkovic, Deborah J. Myers, Michael Ulsh, Scott A. Mauger, *The Impact of Catalyst Ink Dispersing Methodology on Fuel Cell Performance Using In-situ X-ray Scattering,* Chemistry and Nanoscience Center, National Renewable Energy Laboratory, 15013 Denver West Parkway, Golden, Colorado, 80401, United States.

[7] Clayton Jeffery Jacobs, *Influence of catalyst ink mixing procedures on catalyst layer properties and in-situ PEMFC performance,* Centre for Catalysis Research Department of Chemical Engineering University of Cape Town March, 2016.

Nanomaterials Science & Engineering (NMS&E), Vol.2, No.3, 2020

Department of Mechanical Engineering
University of Aveiro
Aveiro 3810-193
Portugal

https://proa.ua.pt/index.php/nmse/

ISSN: 2184-7002

university of aveiro  tema centre for mechanical technology and automation